J. Fluid Mech. (1998), *vol.* 354, *pp.* 1–42.   Printed in the United Kingdom

Nonlinear gravity–capillary waves with forcing and dissipation

By ALEXEY V. FEDOROV AND W. KENDALL MELVILLE
Scripps Institution of Oceanography, University of California San Diego,
La Jolla, CA 92093-0230, USA

(Received 14 February 1997 and in revised form 5 August 1997)

We present a study of nonlinear gravity–capillary waves with surface forcing and viscous dissipation. Based on a viscous boundary layer approximation near the water surface, the theory permits the efficient calculation of steady gravity–capillary waves with parasitic capillary ripples. To balance the viscous dissipation and thus achieve steady solutions, wind forcing is applied by adding a surface pressure distribution. For a given wavelength the properties of the solutions depend upon two independent parameters: the amplitude of the dominant wave and the amplitude of the pressure forcing. We find two main classes of waves for relatively weak forcing: Class 1 and Class 2. (A third class of solution requires strong forcing and is qualitatively different.) For Class 1 waves the maximum surface pressure occurs near the wave trough, while for Class 2 it is near the crest. The Class 1 waves are associated with Miles' (1957, 1959) mechanism of wind-wave generation, while the Class 2 waves may be related to instabilities of the subsurface shear current. For both classes of waves, steady solutions are possible only for forcing amplitudes greater than a certain threshold. We demonstrate how parasitic capillary ripples affect the dissipative and dispersive properties of the solutions. In particular, there may be a significant deviation from the linear phase speed for gravity–capillary waves. Also, wave damping is strongly enhanced by the parasitic capillaries (by as much as two orders of magnitude when compared to the case with no capillary waves). Preliminary experimental results from a wind-wave channel give good agreement with the theory. We find a sharp cut-off in the wavenumber spectra of the solutions which is similar to that observed in laboratory measurements of short gravity–capillary waves. Finally, for large wave amplitudes we find a sharp corner in the wave profile which may separate an overhanging wave crest from a train of parasitic capillaries.

1. Introduction

Cox (1958) undertook the first extensive experiments on the generation of capillary waves by longer waves. Analysing experimental data from a wind-wave tank, he showed that capillary waves form on the forward face of relatively short gravity waves. This has proven to be a common phenomenon occurring at the surface of wind-driven bodies of water. The wavelengths of the dominant waves usually lie in the range 3–15 cm, while the capillary wavelengths range from $O(10^{-1}\text{–}1)$ cm. The capillaries (usually called parasitic capillaries) are stationary or quasi-stationary with respect to the dominant wave. Together they constitute a characteristic asymmetric wave pattern with the ripples on the forward face of the longer wave. The motivation for studying such gravity–capillary waves is based on their importance for air–sea fluxes, especially momentum and gas transfer, and for microwave remote sensing of the ocean surface.

Most widely accepted theories of wind-wave generation (Miles 1957; Phillips 1957) and their extensions neglect such nonlinear effects; however, measurements of wind-generated surface waves by Klinke & Jähne (1997) and Klinke (1996) and preliminary experimental results by A. Rozenberg (private communication) indicate that very soon after the initial stages of wave generation the steepness of gravity waves reaches the threshold necessary for the appearance of the parasitic capillaries. Although small, the capillary ripples influence the dissipative and other dynamical properties of the surface waves. This makes it necessary to include the effects of parasitic capillary waves in any comprehensive theory of wind-wave generation. It is commonly observed that the suppression of capillary waves by surface films can significantly modify the wind-wave field at much longer wavelengths.

Since Cox's experiments, significant progress has been achieved in understanding the dynamics of the interaction between gravity and capillary waves. Theoretical studies of parasitic capillaries include works by Longuet-Higgins (1963), Crapper (1970) and Ruvinsky, Feldstein & Friedman (1991) with extensive reviews by Zhang (1993), Perlin, Lin & Ting (1993) and Longuet-Higgins (1995). The most recent study is by Longuet-Higgins (1996), who related the capillary ripples to a 'leaky' capillary jump near the crest of the gravity wave. Models for the gravity–capillary wave spectrum, based on a Hamiltonian formalism, were proposed by Watson & McBride (1993) and Watson & Buchsbaum (1996). A great deal of experimental research on gravity–capillary waves has been completed, including laboratory studies by Ebuchi, Kawamura & Toba (1987), Perlin *et al.* (1993), Ducan *et al.* (1994*a*, *b*), Zhang & Cox (1994), Zhang (1995), Jähne & Riemer (1990) and Klinke & Jähne (1997), with field measurements by Klinke & Jähne (1995). Dommermuth (1994), and Mui & Dommermuth (1995) have undertaken direct numerical integration of the unsteady Navier–Stokes equations with a free surface. Starting with profiles corresponding to pure gravity waves they obtained solutions with developing parasitic capillaries on the forward face of the waves.

The physical reason for the appearance of the parasitic capillaries is relatively simple, and corresponds to the amplification of higher harmonics of the fundamental waves due to a resonance. The condition of the resonance can be obtained by approximately matching phase speeds between the longer wave and the shorter capillary wave. Nonlinearity, dissipation and forcing may further complicate the process. For example, nonlinearity leads to the local resonant condition being different for different phases of the longer-wave profile.

The most comprehensive theoretical explanation of the phenomenon so far was given in the recent study by Longuet-Higgins (1995). He considered a steady model with several physically motivated assumptions, the most important of which were:

(i) In the first approximation, the underlying wave is a pure gravity wave and is given by a Stokes expansion.

(ii) Surface tension and the high curvature localized at the crest of the gravity wave act as a forcing term.

(iii) Parasitic capillaries appear as a linear response to the local forcing and ride on the Stokes wave as if on a slowly varying current in a slowly varying gravitational field.

(iv) The parasitic capillaries are damped by viscosity.

Despite good qualitative agreement with observations, this and earlier models are unable to reproduce several features of gravity–capillary waves with parasitic capillaries. These include the fact that parasitic capillary waves may become strongly nonlinear features of the surface with large slopes, and that capillary waves are known to generate a strong vorticity field that may interact with the waves (see Longuet-Higgins 1953, 1992*b*, 1994; Ebuchi *et al.* 1987). In some cases the wave crest bulges forward, giving a surface that may become multi-valued in the horizontal coordinates. Longuet-Higgins (1992*b*) referred to this bulge as a capillary roller. According to Ebuchi *et al.* (1987) the capillary roller may be a region of high vorticity. The bulge and the train of capillary waves are separated by a sharp corner in the profile of the free surface (see figures 5*b* and 10*b* below). The latter feature has not been accounted for by any theory, although it has recently been seen in numerical results by Longuet-Higgins & Dommermuth (1997) on inviscid wave crest instabilities. A semi-quantitative explanation of the bulge as a solitary wave trapped on a velocity gradient was given by Longuet-Higgins (1996). Finally, the earlier models do not include the action of wind which is the major source of waves in the ocean.

In our approach we are able to calculate nonlinear gravity–capillary waves with wind forcing and dissipation accurately and efficiently, while taking into account the underlying vorticity field. Our approach follows the classical boundary layer approximation, assuming, in the first approximation, that the flow is irrotational. The effect of a viscous boundary layer is included at the next order, allowing for a rotational correction in a boundary layer adjacent to the surface. Thus, the main ideas and assumption of our model can be summarized as follows:

(i) The flow is irrotational everywhere except in a thin subsurface viscous boundary layer.

(ii) Irrotational flow is used to describe the gravity–capillary waves in the first approximation. Additional terms due to the presence of the viscous boundary layer are calculated. The effects of the new terms on the original irrotational variables and surface profile are found.

(iii) Fully nonlinear boundary conditions are invoked in order to calculate nonlinear capillary waves.

(iv) Steady waves are considered and a complete Stokes expansion with complex coefficients is utilized. The irrotational velocity potential and streamfunction of the first approximation are used as the independent variables. This part of our approach is similar to calculations of steady gravity and gravity–capillary waves by Chen & Saffman (1980), Zufiria (1987), Debiane & Kharif (1996) and others. (In effect, we have generalized the method of Chen & Saffman for pure gravity–capillary waves to include wave damping and external forcing. Ruvinsky *et al.* (1991) is another study, which dealt with gravity–capillary waves with viscous dissipation).

(v) Simple atmospheric forcing, needed for the waves to remain steady and periodic, is explicitly included in the model.

Using this approach we formulate a closed set of equations for the elevation of the free surface. The equations are discretized and a truncated Stokes series is used to obtain a set of algebraic equations for the Stokes coefficients. This set is solved numerically by Newton's method. Owing to the complicated form of our equations, we calculate the Jacobian for Newton's method numerically, rather than analytically as in other studies (e.g. Chen & Saffman 1980; Longuet-Higgins 1993).

Asymmetric solutions with parasitic capillary waves appearing on the forward face of the dominant wave are computed for different wave heights and different amplitudes of the pressure forcing. The calculations are conducted for wavelengths of the dominant wave in the interval 4–12 cm. (At larger scales the parasitic capillaries have relatively small amplitudes). The strength of the parasitic capillary waves increases with increasing amplitude of the dominant wave, so that the capillary ripples rapidly become nonlinear.

For the forcing we use a cosine pressure distribution at the surface with the length scale equal to the wavelength of the dominant wave. As long as the pressure forcing remains weak, we find two main classes of solutions (Class 1 and Class 2). There exist other qualitatively different solutions which require relatively strong forcing (see Appendix A). The major difference between the two main types of solutions is that for the Class 1 waves the maximum surface pressure occurs near the wave trough, while for the Class 2 ones it occurs near the crest. The Class 1 waves can be associated with Miles' (1957, 1959) mechanism of wind-wave generation by an instability of the shear air flow above the water surface. The Class 2 waves may be related to surface wave generation by instabilities of sub-surface shear flows (Morland, Saffman & Yuen 1991; Shrira 1993). Both classes of waves share certain similarities, but have some important distinctions, especially for larger wave amplitudes and larger pressure forcing.

For both classes of solution, for each particular wave height there is a minimum amplitude of the forcing necessary for steady solutions to exist. Clearly, the amplitude and wavelength of the parasitic capillaries depend upon the value of the pressure forcing. If one increases the forcing amplitude together with the amplitude of the dominant wave, the capillary waves become more nonlinear. However, if one increases the forcing amplitude, while keeping the amplitude of the dominant wave fixed, the capillary waves become stronger only for the Class 1 solutions, but weaken for the Class 2 waves. Importantly, the forcing, together with nonlinear effects, lead to significant deviations from the dispersion relationship for linear gravity–capillary waves.

We calculate energy spectra for the solutions and find that each spectrum has a characteristic cut-off with an abrupt decrease in spectral density by two to eight orders of magnitude. The cut-off takes place immediately after the local peak in the spectra corresponding to parasitic capillaries. According to the measurements by Klinke & Jähne (1995, 1997), Klinke (1996) and others the most typical cut-off wavenumber for wind waves is around 1000 rad m^{-1}, corresponding to 6 mm wavelength. In our solutions this cut-off wavenumber occurs in the energy spectrum for a dominant wavelength of 4 cm. Finally, we compare our solutions with preliminary experimental results from a wind-wave channel.

The structure of the paper is as follows. In §2 we introduce the governing equations and outline the boundary layer approximation and linear damping. Most of the mathematical derivations are completed in §§3–5, which include consideration of the vorticity advection–diffusion equation and the derivation of Bernoulli's integral for weakly damped flows. In §6 we combine all the analytical expressions and give the final mathematical formulation of the problem. In §7 we show how to calculate the energy density and energy dissipation associated with the waves. In §8 we give a linear approximation to the problem with a physical interpretation of the pressure forcing, which leads to the introduction of the Class 1 and Class 2 solutions. In the same section we discuss the relation of these solutions to different mechanisms of wind-wave generation. Our numerical results are presented in §§9–13, including the profiles of the free surface, dissipation estimates, and comparison with preliminary experimental results. The reader who is so inclined can go directly to §6 or even §9 to avoid the mathematical development.

In addition, we provide the following clarification of the terminology we use in the paper.

Gravity–capillary waves: nonlinear surface waves for which both gravity and surface tension are important. In the parameter range we are using, they are characterized by the existence of two major scales: the longer scale coincides with the entire wavelength, and the shorter scale is due to a harmonic resonance. This shorter scale is observed as capillary ripples for which the effect of the surface tension is more important than gravity.

Fundamental wave: the first Stokes harmonic of the appropriate Stokes expansion for the gravity–capillary wave of a fixed wavelength.

Dominant wave (longer wave): a gravity–capillary wave with parasitic capillary ripples filtered out. The dominant wave can be approximated by taking the Stokes harmonics before the local maximum associated with the parasitic capillaries. See §10. Importantly, the dominant wave is still influenced by surface tension.

The separation of the wave into the dominant part and capillary ripples is convenient, and provides a physical interpretation of the phenomenon. However, in fact, there exists only one nonlinear wave, or wave system, in which capillaries are higher harmonics of the fundamental waves.

2. Basic equations, the boundary layer approximation and other assumptions

Potential-flow theory has been the traditional tool for studying gravity and capillary–gravity waves on deep water. There have been many studies validating this theory in different cases (e.g. Dommermuth *et al.* 1988). However, in several important applications the flow near the surface cannot be considered irrotational. Since the fluid has a small, but non-zero viscosity (Longuet-Higgins 1992*a*, *b*, 1994), the free surface generates a vorticity field, which increases with increasing curvature of the free surface. Usually the vorticity remains localized in a subsurface layer which is thin compared to the characteristic wavelength. (For other examples of rotational surface waves see Milinazzo & Saffman 1990; Fedorov & Melville 1997).

To treat periodic surface waves of permanent form we transform to a frame of reference travelling with speed c to the right ($c > 0$). In the new reference frame the motion is steady, and we let x and y be the horizontal and vertical coordinates, respectively. When presenting the results, the origin of y will be shifted to let the mean surface elevation be zero, but at this point it is arbitrary. The waves are considered two-dimensional in space, i.e. the elevation of the free surface varies only with x, while the flow velocities depend upon x and y.

Following Longuet-Higgins (1992*b*), we introduce a characteristic thickness of the surface boundary layer (see figure 1) as

$$\delta \sim (2\nu/\sigma)^{1/2} \tag{2.1}$$

where $\sigma = ck$ is the radian frequency, ν the kinematic viscosity, $k = 2\pi/\lambda$ the wavenumber and λ is the wavelength for surface waves. For subsequent boundary layer approximations we require that

$$\gamma = k\delta \ll 1. \tag{2.2}$$

Note that the local thickness of the boundary layer δ_e (see §3) will vary with the horizontal coordinate, but its value remains of the same order of magnitude as δ.† Also the estimates (2.1) and (2.2) imply that $\gamma \propto \nu^{1/2}$.

---

† Strictly speaking, we should introduce two local thicknesses of the boundary layer: one due to capillary waves, the other due to the dominant wave. The maximum of the two determines the actual thickness of the boundary layer. However, γ will not enter the final equation explicitly, and this will not affect our derivations.

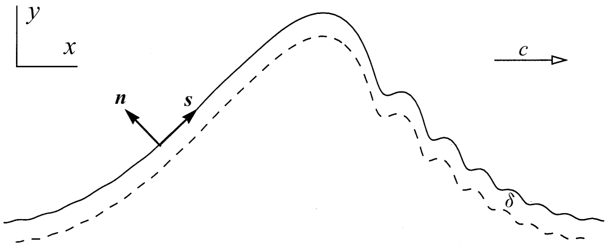

FIGURE 1. A surface wave with parasitic capillaries riding on the forward face of the longer wave. Also shown are the viscous boundary layer near the surface and the natural coordinate system (s, n). The thickness of the boundary layer is δ; $\gamma = k\delta \ll 1$. (The figure is not to scale, and, in fact, δ is assumed to be much smaller than the characteristic wavelength of capillary ripples.)

Next, we introduce natural coordinates (s, n), where $\boldsymbol{s}$ and $\boldsymbol{n}$ are unit vectors along and normal to the surface, respectively. The scaling factors (Batchelor 1967, p. 598) connecting them to the usual rectilinear coordinates are (Longuet-Higgins 1953)

$$h^{(s)} = h = 1+\frac{n}{R}, \quad h^{(n)} = 1, \tag{2.3}$$

where $R = R(s)$ is the local radius of curvature of the water surface, positive at the wave crests. More generally R is the radius of curvature for the streamlines. Since we are considering a thin boundary layer, we can disregard the dependence of R upon n within the boundary layer. Note that at the surface itself $h(s, 0) = 1$.

The usual expression for R is

$$\frac{1}{R} = \frac{X_{ss}\,Y_s - X_s\,Y_{ss}}{(X_s^2+Y_s^2)^{3/2}}, \tag{2.4}$$

where

$$X = X(s), \quad Y = Y(s) \tag{2.5}$$

is a parametric representation of the surface. Instead of s we can choose any other independent parameter, as the form of (2.4) does not change under transformations of the independent parameter (Korn & Korn 1968).

In the new coordinates the steady motion within the boundary layer is determined by the vorticity equation and mass conservation:

$$u\frac{\partial \omega}{\partial s}+vh\frac{\partial \omega}{\partial n} = \nu\left(\frac{\partial}{\partial s}\left(\frac{1}{h}\frac{\partial \omega}{\partial s}\right)+\frac{\partial}{\partial n}\left(h\frac{\partial \omega}{\partial n}\right)\right), \tag{2.6}$$

and

$$\frac{\partial u}{\partial s}+\frac{\partial (vh)}{\partial n} = 0, \tag{2.7}$$

where

$$\omega = \frac{1}{h}\left(\frac{\partial v}{\partial s}-\frac{\partial (uh)}{\partial n}\right). \tag{2.8}$$

Here, $\boldsymbol{u} = \boldsymbol{u}(s, n)$ is the fluid velocity, $\boldsymbol{u} = (u, v)$, P the pressure, ρ the fluid density, g gravity, y the vertical coordinate, and ω the vorticity of the flow.

Equations (2.6)–(2.8) are supplemented by the generalized Bernoulli equation for steady viscous flow:

$$\frac{\partial}{\partial s}\left(\frac{u^2}{2}+\frac{P}{\rho}+gy\right)+\nu\frac{\partial \omega}{\partial n} = 0 \quad \text{at} \quad n = 0. \tag{2.9}$$

Equation (2.9) is a consequence of momentum conservation along s (Lugt 1987).

The dynamic boundary conditions on the surface are the continuity of the normal and tangential stresses, respectively (Landau & Lifshitz 1987),

$$\frac{P}{\rho}+2\nu\frac{\partial u}{\partial s}=\frac{P_0}{\rho}+\frac{T}{R} \tag{2.10}$$

and

$$\frac{\tau}{\rho}=\nu\frac{\partial}{\partial n}\left(\frac{u}{h}\right)=0, \tag{2.11}$$

where T is the surface tension and P_0 is the external atmospheric pressure, necessary to supply the energy to keep the waves steady. P_0 is a function of the horizontal coordinate x. The kinematic boundary condition on the surface is

$$v=0 \quad \text{at} \quad n=0, \tag{2.12}$$

which is equivalent to

$$\psi=0 \quad \text{at} \quad n=0, \tag{2.13}$$

where the streamfunction ψ is introduced so that

$$u=\frac{\partial\psi}{\partial n}, \quad v=-\frac{1}{h}\frac{\partial\psi}{\partial s}. \tag{2.14}$$

Finally note that outside the boundary layer the flow is irrotational, with

$$\omega\rightarrow 0 \quad \text{and} \quad u\rightarrow -c \quad \text{as} \quad y\rightarrow -\infty. \tag{2.15}$$

We express the streamfunction ψ and the velocity $\boldsymbol{u}$, as well as the elevation of the free surface η, each as sums of two terms, with one part corresponding to the ideal flow and a correction due to the viscous boundary layer:

$$\psi=\psi^i+\psi^b, \tag{2.16}$$

$$\boldsymbol{u}=\boldsymbol{u}^i+\boldsymbol{u}^b, \tag{2.17}$$

and

$$\eta=\eta^i+\eta^b. \tag{2.18}$$

For the ideal part of the flow we also introduce the potential ϕ^i. The parametric description of the surface is now

$$X=X^i+X^b; \quad Y=Y^i+Y^b, \tag{2.19}$$

where all (X^i, Y^i) and (X^b, Y^b) are functions of s. Clearly, Y and η differ only by an arbitrary constant, but for convenience we will use both notations. Also, according to our definition of the irrotational terms and rotational corrections, and according to formula (2.8) for ω, in the interior of the flow

$$\omega=\frac{1}{h}\left(\frac{\partial v^b}{\partial s}-\frac{\partial(u^b h)}{\partial n}\right), \tag{2.20}$$

and

$$\frac{\partial v^i}{\partial s}-\frac{\partial(u^i h)}{\partial n}=0. \tag{2.21}$$

It can be shown that (Ruvinsky *et al.* 1991; Longuet-Higgins 1992*b*)

$$u^b \sim \gamma, \quad v^b \sim \gamma^2, \quad \psi^b \sim \gamma^2, \tag{2.22}$$

and consequently $\eta^b \sim \gamma^2$. Also $\delta/R = O(\gamma)$. As long as γ is small, this implies that the boundary layer corrections are small compared to the ideal parts of the flow.

If $\nu = 0$ and $\omega = 0$, all the boundary terms vanish, and Euler's description of the irrotational surface waves is recovered from (2.6)–(2.11). The boundary condition (2.11) is satisfied identically, and integrating (2.9) with respect to s gives Bernoulli's integral at the surface,

$$\frac{u^{i2}}{2}+gY^i+\frac{T}{R}+\frac{P_0}{\rho} = \text{const.} \tag{2.23}$$

The kinematic boundary condition remains the same:

$$\psi^i = 0 \quad \text{at} \quad n = 0, \tag{2.24}$$

and $\omega = 0$ implies that

$$\nabla^2\psi^i = 0 \tag{2.25}$$

everywhere in the fluid. Thus, (2.25), together with (2.23) and (2.24), gives a standard description of surface gravity–capillary waves with no viscosity. Now our task is to correct this set of equations to allow for small viscosity. Accordingly, in the next sections we will express boundary layer corrections in (2.6)–(2.11) in terms of the ideal irrotational flow.

Finally, we need one more assumption. We introduce ϵ as a measure of the relative characteristic slope of the free surface

$$\epsilon = \max(\epsilon_d, \epsilon_c), \tag{2.26}$$

where ϵ_d and ϵ_c are the characteristic slopes of the dominant wave and capillary ripples, respectively. The slopes are defined as

$$\epsilon_d = ak, \quad \epsilon_c = a_c k_c, \tag{2.27}$$

where a and a_c are characteristic amplitudes of the dominant wave and capillary ripples, respectively, k is the wavenumber based on the length of the dominant wave, and k_c is the wavenumber based on the wavelength of the capillary ripples.

Now we adopt the assumption of linear friction, i.e. in describing weak frictional effects, and only frictional effects, we will keep terms proportional to ϵ, but neglect terms proportional to ϵ^2. This assumption is equivalent to classical linear† damping (Phillips 1977; Lighthill 1978) and implies that all Fourier harmonics of the wave are damped independently. Provided ϵ is small, one can easily show that (Whitham 1974; Phillips 1977; Longuet-Higgins 1992*b*, also see (2.4))

$$u \approx -c, \quad |c+u| \sim \epsilon, \quad \eta \sim \epsilon, \quad u_s \sim \epsilon, \quad X_s \approx 1, \quad \frac{1}{R} \approx -Y_{ss} \sim \epsilon. \tag{2.28}$$

(These expressions are well-known in the linear theory of surface waves.) The smallness of ϵ and estimates of this kind will be used only in evaluating the damping terms. For higher values of ϵ, consideration of the higher-order dissipative terms may become necessary, but their relative importance remains an open question (see also the final remark of §9).

---

† We need to emphasize that in this case 'linear' does not actually mean that the friction terms are linear functions of surface velocity for example, as is used in some simple models.

3. Vorticity field near the free surface

First, we study the vorticity field associated with the damped gravity–capillary waves and consider a formulation to leading order in γ. Using the mass conservation equation (2.7) with the kinematic boundary condition (2.12) we find that in the boundary layer

$$v = -\frac{\partial U^i}{\partial s} n, \tag{3.1}$$

where

$$U = U(s) = U^i + U^b \tag{3.2}$$

is the flow velocity at the surface. With (3.1) the vorticity equation (2.6) reduces to

$$U^i \frac{\partial \omega}{\partial s} - \frac{\partial U^i}{\partial s} n \frac{\partial \omega}{\partial n} = \nu \frac{\partial^2 \omega}{\partial n^2}. \tag{3.3}$$

Combining (2.3), (2.8), (2.11) and (2.12) yields the vorticity immediately at the free surface as

$$\omega|_{n=0} = -2U/R \tag{3.4}$$

or to leading order

$$\omega|_{n=0} \approx -2U^i/R^i, \tag{3.5}$$

where R^i is calculated as in (2.4) but in terms of X^i and Y^i. This result is due to Longuet-Higgins (1953, 1992*b*, see also Batchelor 1967 and Phillips 1977).

To solve (3.3) with the boundary condition (3.5) we introduce new variables

$$\zeta = -\frac{k}{c}\int U^i \, \mathrm{d}s = -\frac{k}{c}\phi^i \tag{3.6}$$

and

$$r = -\frac{k}{c} U^i n. \tag{3.7}$$

(Later we will use ζ as the independent variable for parametrizing the free surface.) One can easily verify that in these new variables the vorticity equation becomes linear:

$$-\frac{\partial \omega}{\partial \zeta} = \frac{k\nu}{c}\frac{\partial^2 \omega}{\partial r^2} \tag{3.8}$$

with

$$\omega|_{r=0} = -2U^i/R^i. \tag{3.9}$$

A solution of (3.8)–(3.9) periodic in ζ can be written as

$$\omega = \omega_1 + \bar{\omega} \tag{3.10}$$

where

$$\omega_1 = \mathrm{Re}\left\{ \sum_{m=1}^{\infty} q_m \exp\left[-\mathrm{i}\zeta m + (1+\mathrm{i})\, r \left(\frac{mc}{2\nu k} \right)^{1/2} \right] \right\}, \tag{3.11}$$

with the Fourier coefficients q_m:

$$q_m = \frac{1}{\pi}\int_0^{2\pi} \left(-\frac{2U^i}{R^i} + \left\langle \frac{2U^i}{R^i} \right\rangle \right) \mathrm{e}^{\mathrm{i}\zeta' m} \, \mathrm{d}\zeta', \tag{3.12}$$

and $\bar{\omega}$ given by

$$\bar{\omega} = \left\langle -\frac{2U^i}{R^i} \right\rangle = \frac{1}{2\pi}\int_0^{2\pi}\left(-\frac{2U^i}{R^i}\right)\mathrm{d}\zeta'. \tag{3.13}$$

Without loss of generality we have assumed that the wave is 2π-periodic in ζ. The $\langle \ldots \rangle$ denotes the average over a wavelength with respect to ζ.

While ω_1 is exponentially decaying with r (i.e. with depth), $\bar{\omega}$ is a non-zero constant (for nonlinear waves). Thus at the lower edge of the boundary layer the vorticity has some non-zero value. Formally, we must subtract this constant in (3.12) for ω_1 to be finite everywhere.

The component $\bar{\omega}$, the so-called rectified vorticity, was first introduced by Longuet-Higgins (1953, 1992*b*, see also Batchelor 1967; Mei 1983) although in a less general form. This rectified vorticity should diffuse into the interior of the fluid resulting in a growing shear current beneath the wave (Longuet-Higgins 1992*b*). Similarly, the shear stress from the wind contributes to this shear current, which may affect the waves but on longer time scales. In our calculations these effects are neglected, which is justifiable for moderate wave amplitudes and wind speeds, or for shorter time scales.

With the use of (2.28) and (3.11)–(3.13) one can easily show that

$$\omega_1 \sim \epsilon, \quad \text{but} \quad \bar{\omega} \sim \epsilon^2, \tag{3.14}$$

so that $\bar{\omega}$ remains a variable of second order in ϵ. Following the assumption of linear friction in §2 and a remark in the previous paragraph, we will neglect $\bar{\omega}$ further and replace ω with ω_1.

From (3.11) with (3.7) we calculate the dimensional local thickness of the boundary layer, based on the exponential decay scale, as

$$\delta_e = \left(\frac{2\nu}{ck}\right)^{1/2}\frac{c}{|U^i|} = \delta\frac{c}{|U^i|}. \tag{3.15}$$

That is, the thickness of the boundary layer is modulated by the factor $c/|U^i|$ from δ. If there is a stagnation point at the surface, the boundary layer becomes infinitely large, which may correspond to flow separation.

For later use, we calculate ψ^b at the surface. From (2.14), (2.16), (2.17) and (2.20) to leading order in γ

$$\psi^b = -\int_{-\infty}^{0}\int_{-\infty}^{n}\omega\,\mathrm{d}n\,\mathrm{d}n. \tag{3.16}$$

Introducing

$$I = \int_{-\infty}^{0}\int_{-\infty}^{r}\omega\,\mathrm{d}r\,\mathrm{d}r \tag{3.17}$$

gives

$$\psi^b \approx -\frac{c^2}{k^2 U^{i2}} I \approx -\frac{I}{k^2}. \tag{3.18}$$

The value of I is obtained through integrating (3.8) twice and neglecting terms of second order in ϵ:

$$-\frac{\partial I}{\partial \zeta} = \frac{k\nu}{c}\,\omega|_{r=0} \approx \frac{k\nu}{c}\,\omega_1|_{r=0} \tag{3.19}$$

and

$$I \approx -\frac{k\nu}{c}\int_0^{\zeta}\omega_1|_{r=0}\,\mathrm{d}\zeta' = \frac{2k\nu}{c}\int_0^{\zeta}\left(\frac{U^i}{R^i} - \left\langle\frac{U^i}{R^i}\right\rangle\right)\mathrm{d}\zeta', \tag{3.20}$$

where again the symbol $\langle \ldots \rangle$ stands for the average over a wavelength with respect to ζ. Formula (3.20) for I corresponds to our solution (3.11) for ω_1.

4. Bernoulli's integral for a weakly damped flow

Now we are ready to derive Bernoulli's integral for a weakly damped flow. Rewriting (2.9) with (2.10) yields

$$\frac{\partial}{\partial s}\left(\frac{U^2}{2}+gY+\frac{T}{R}+\frac{P_0}{\rho}-2\nu\frac{\partial U}{\partial s}\right)+\nu\frac{\partial \omega}{\partial n}=0 \quad \text{at} \quad n=0. \tag{4.1}$$

Integrating the vorticity equation (2.6) with (2.15) with respect to n from $-\infty$ to zero, using integration by parts, and applying mass conservation (2.7) yields (at the surface)

$$\nu\frac{\partial \omega}{\partial n}=\frac{\partial}{\partial s}\int_{-\infty}^{0}(u\omega)\,\mathrm{d}n-\nu\frac{\partial}{\partial s}\int_{-\infty}^{0}\frac{1}{h}\frac{\partial \omega}{\partial s}\mathrm{d}n \tag{4.2}$$

or, to leading order in γ,

$$\nu\frac{\partial \omega}{\partial n}\approx\frac{\partial}{\partial s}\int_{-\infty}^{0}(u\omega)\,\mathrm{d}n, \tag{4.3}$$

since

$$\nu\propto\gamma^2, \quad \int_{-\infty}^{0}\omega\,\mathrm{d}n\sim\delta\sim\gamma, \quad \nu\frac{\partial}{\partial s}\int_{-\infty}^{0}\frac{1}{h}\frac{\partial \omega}{\partial s}\mathrm{d}n\sim\gamma^3. \tag{4.4}$$

We replace u and ω with their expressions from (2.17) and (2.20) and neglect the terms of order γ^2 and higher to obtain

$$\nu\frac{\partial \omega}{\partial n}=\frac{\partial}{\partial s}\int_{-\infty}^{0}(u^i+u^b)\frac{1}{h}\left(\frac{\partial v^b}{\partial s}-\frac{\partial(u^b h)}{\partial n}\right)\mathrm{d}n \tag{4.5}$$

$$\approx-\frac{\partial}{\partial s}\int_{-\infty}^{0}(u^i+u^b)\frac{1}{h}\frac{\partial(u^b h)}{\partial n}\mathrm{d}n\approx-\frac{\partial}{\partial s}\left(\int_{-\infty}^{0}\frac{u^i}{h}\frac{\partial(u^b h)}{\partial n}\mathrm{d}n+\frac{U^{b2}}{2}\right) \tag{4.6}$$

(integrating by parts)

$$=\frac{\partial}{\partial s}\left(\int_{-\infty}^{0}u^b h\frac{\partial(u^i/h)}{\partial n}\mathrm{d}n-\frac{U^{b2}}{2}-U^iU^b\right)$$

$$\approx\frac{\partial}{\partial s}\left(\int_{-\infty}^{0}u^b\frac{\partial u^i}{\partial n}\mathrm{d}n-\int_{-\infty}^{0}\frac{u^iu^b}{R}\mathrm{d}n-\frac{U^{b2}}{2}-U^iU^b\right). \tag{4.7}$$

In the boundary layer (see (2.3), (2.12), (2.21) and (2.22))

$$\frac{\partial u^i}{\partial n}\approx-\frac{u^i}{R'} \tag{4.8}$$

that is,

$$\nu\frac{\partial \omega}{\partial n}\approx-\frac{\partial}{\partial s}\left(\frac{U^{b2}}{2}+U^iU^b\right). \tag{4.9}$$

Substituting (4.9) in (4.1) and neglecting terms of higher order gives

$$\frac{\partial}{\partial s}\left(\frac{U^{i2}}{2}+gY+\frac{T}{R}+\frac{P_0}{\rho}-2\nu\frac{\partial U^i}{\partial s}\right)=0 \quad \text{at} \quad n=0, \tag{4.10}$$

or after integrating (4.10),

$$\frac{U^{i2}}{2}+gY+\frac{T}{R}+\frac{P_0}{\rho}-2\nu\frac{\partial U^i}{\partial s}=E \quad \text{at} \quad n=0, \tag{4.11}$$

where E is an arbitrary constant. Now replacing s with ζ in (4.11) yields

$$\frac{U^{i2}}{2}+gY+\frac{T}{R}+\frac{P_0}{\rho}+\frac{\nu k}{c}\frac{\partial}{\partial\zeta}U^{i2}=E \quad \text{at} \quad n=0, \tag{4.12}$$

This is Bernoulli's integral for a weakly damped flow. Now we need to recalculate both Y and R in terms of X^i and Y^i, as they include boundary layer corrections.

5. The change of the elevation and curvature of the free surface due to the boundary layer corrections

To calculate the boundary layer corrections in both the elevation Y and curvature $1/R$, we introduce a 'virtual' surface (figure 2) parametrically described as

$$X^i = X^i(s), \quad Y^i = Y^i(s). \tag{5.1}$$

It can be defined as the surface where $\psi^i = 0$. The real surface is described as

$$X = X(s), \quad Y = Y(s), \tag{5.2}$$

or it can be similarly defined as $\psi = 0$.

Let $\boldsymbol{n}^b = \boldsymbol{n}^b(s)$ be a vector connecting the real and the virtual surfaces (see figure 2). We calculate n^b, using a Taylor expansion for ψ^i. At the real surface

$$\psi^i \approx \frac{\partial\psi^i}{\partial n}n^b \approx U^i n^b, \tag{5.3}$$

but from (2.16)

$$\psi^i = -\psi^b. \tag{5.4}$$

Combining these two expressions gives

$$n^b \approx -\psi^b/U^i. \tag{5.5}$$

One should immediately notice that $n^b \sim \gamma^2$, and $|n^b| \ll \delta$. That is, the boundary layer thickness is much larger than the depth of the virtual surface. In addition, an expression for ψ^b in (5.5) was obtained in §3 ((3.18) and (3.20)).

Now recalling that the difference between the real and virtual surfaces is just the boundary layer correction, and projecting $\boldsymbol{n}^b$ onto the horizontal and vertical axes gives

$$Y^b = n^b \cos\hat{\alpha} \tag{5.6}$$

and

$$X^b = -n^b \sin\hat{\alpha}, \tag{5.7}$$

where $\hat{\alpha}$ is the angle of inclination of the surface to the horizontal. Using ζ instead of s for parametrizing the surface gives

$$\cos\hat{\alpha} \approx X^i_s = -\frac{kU^i}{c}X^i_\zeta \tag{5.8}$$

and

$$\sin\hat{\alpha} \approx Y^i_s = -\frac{kU^i}{c}Y^i_\zeta. \tag{5.9}$$

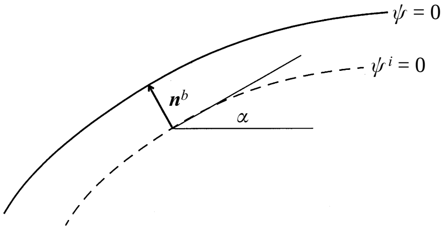

FIGURE 2. The real surface described by $\psi = 0$ and the virutal surface $\psi^i = 0$. The connection is given by the vector $\boldsymbol{n}^b$. Note that $|n^b| \ll \delta$. (The figure is not to scale.)

We combine (5.6)–(5.8) and (5.7)–(5.9) to yield

$$Y^b = \frac{k\psi^b}{c} X^i_\zeta \tag{5.10}$$

and

$$X^b = -\frac{k\psi^b}{c} Y^i_\zeta. \tag{5.11}$$

Introducing

$$Z = X + \mathrm{i}Y, \quad Z^i = X^i + \mathrm{i}Y^i, \quad Z^b = X^b + \mathrm{i}Y^b \tag{5.12}$$

gives

$$Z^b = \frac{\mathrm{i}k\psi^b}{c} Z^i_\zeta, \tag{5.13}$$

and

$$Z = Z^i + \frac{\mathrm{i}k\psi^b}{c} Z^i_\zeta. \tag{5.14}$$

Since

$$|Z^i_\zeta| = \left|\frac{Z^i_s}{\zeta_s}\right| \approx \frac{1}{\zeta_s} = \frac{c}{U^i k} \approx \frac{1}{k} \tag{5.15}$$

and

$$\psi^b \approx -I/k^2 \tag{5.16}$$

(see §3, (3.18) and (3.20)), in the approximation of linear friction we write

$$Z \approx Z^i - \frac{\mathrm{i}I}{k^2 c}, \tag{5.17}$$

which allows us to calculate the elevation of the surface Y. Knowing Z, the curvature $1/R$ can be computed as (cf. (2.4))

$$\frac{1}{R} = -\mathrm{Im}\{Z_{\zeta\zeta} Z_\zeta^{-3/2} Z_\zeta^{*-1/2}\}, \tag{5.18}$$

where the asterisk denotes the complex conjugate.

There are still two more problems to resolve. First, the velocity U^i is different at the real and virtual surfaces. The difference ΔU^i is given by a Taylor expansion, along with (2.28), (4.8) and (5.5),

$$\Delta U^i \approx \frac{\partial U^i}{\partial n} n^b \approx -\frac{U^i}{R} n^b \approx \frac{\psi^b}{R} \sim \gamma^2 \epsilon^2, \tag{5.19}$$

so that in the linear friction approximation it can be neglected.

Finally, it will be necessary to express U^i in terms of X^i and Y^i:

$$U^i = -\frac{c}{k}\bigg/\frac{\mathrm{d}s}{\mathrm{d}\zeta} \approx -\frac{c}{k(X_\zeta^{i2}+Y_\zeta^{i2})^{1/2}}, \tag{5.20}$$

or

$$U^i = -\frac{c}{k}(Z_\zeta^i Z_\zeta^{i*})^{-1/2}. \tag{5.21}$$

This concludes our preliminary calculations.

6. Final formulation of the problem and numerical approach

In the previous sections we calculated Bernoulli's integral for weakly damped flows. Now following a standard approach (Chen & Saffman 1980; Longuet-Higgins 1984; Zufiria 1987) we represent the ideal part of wave motion in the fluid by means of a Stokes expansion

$$kz^i = -\frac{\phi^i+\mathrm{i}\psi^i}{c}k + \mathrm{i}\sum_{m=1}^{\infty} a_m \,\mathrm{e}^{\mathrm{i}m\frac{\phi^i+\mathrm{i}\psi^i}{c}k}. \tag{6.1}$$

Here, the complex potential $\phi^i + \mathrm{i}\psi^i$ is used as a complex independent variable for describing the motion. Expression (6.1) is a consequence of the complex potential being an analytic function of z^i, or alternatively, z^i being analytic function of the complex potential. Complex factors a_m are Fourier coefficients to be determined (Stokes coefficients). If the a_m are zeros then the motion is a steady uniform flow to the left that is determined by a simple complex potential (remember that we sit in the frame of reference travelling to the right)

$$\phi^i + \mathrm{i}\psi^i = -cz^i. \tag{6.2}$$

Clearly, non-zero a_m correspond to a superposed wave motion.

On the virtual surface $\psi^i = 0$, and (6.1) gives a parametric representation for Z^i:

$$kZ^i = -\frac{\phi^i}{c}k + \mathrm{i}\sum_{m=1}^{\infty} a_m \,\mathrm{e}^{\mathrm{i}m\frac{\phi^i}{c}k} = \zeta + \mathrm{i}\sum_{m=1}^{\infty} a_m \,\mathrm{e}^{-\mathrm{i}m\zeta}. \tag{6.3}$$

Now combining equations (3.13), (3.20), (4.12), (5.17), (5.18), (5.21) and (6.3) leads to the final formulation of the problem: find Z^i, such that

$$Z^i = \frac{1}{k}\left(\zeta + \mathrm{i}\sum_{m=1}^{\infty} a_m \,\mathrm{e}^{-\mathrm{i}m\zeta}\right), \quad \zeta \subset [0, 2\pi], \tag{6.4}$$

and

$$\frac{U^{i2}}{2} + gY + \frac{T}{R} + \frac{P_0}{\rho} + \frac{\nu k}{c}\frac{\partial}{\partial\zeta}U^{i2} = E, \tag{6.5}$$

where

$$U^i = -\frac{c}{k}(Z_\zeta^i Z_\zeta^{i*})^{-1/2}, \tag{6.6}$$

$$Z = Z^i - \frac{2\nu\mathrm{i}}{c^2 k}\int_0^\zeta \left(\frac{U^i}{R^i} - \left\langle\frac{U^i}{R^i}\right\rangle\right)\mathrm{d}\zeta', \tag{6.7}$$

$$\frac{1}{R} = -\,\mathrm{Im}\,\{Z_{\zeta\zeta} Z_\zeta^{-3/2} Z_\zeta^{*-1/2}\}, \tag{6.8}$$

$$P_0 = \tilde{P}_0 \cos kX, \tag{6.9}$$

with

$$X = \operatorname{Re} Z - \operatorname{Re} Z|_{\zeta=0}, \quad Y = \operatorname{Im} Z, \tag{6.10}$$

$$\frac{1}{R^i} = -\operatorname{Im}\{Z^i_{\zeta\zeta} Z^{i-3/2}_{\zeta} Z^{i*-1/2}_{\zeta}\}, \tag{6.11}$$

and

$$\left\langle \frac{U^i}{R^i} \right\rangle = \frac{1}{2\pi} \int_0^{2\pi} \frac{U^i}{R^i} \mathrm{d}\zeta'. \tag{6.12}$$

In (6.10) we have additionally subtracted a constant ($\operatorname{Re} Z|_{\zeta=0}$) in order to fix the reference point with respect to x. Finally, we introduce the wave amplitude as

$$a = \frac{\max(Y) - \min(Y)}{2}, \tag{6.13}$$

corresponding to the characteristic slope of the longer wave ak. Equations (6.4)–(6.13) must be solved for a_m, c and E with a and $\tilde{P}_0$ as independent parameters. As soon as a_m, c and E are found, Z^i is calculated from (6.4) and Z from (6.7). This gives the profile of the free surface uniquely. Note that the system (6.4)–(6.13) is equivalent to one equation, which can be written as

$$Q(\zeta, c, E, a_1, a_2, a_3, \ldots) = 0, \quad \zeta \subset [0, 2\pi], \tag{6.14}$$

where Q is some nonlinear operator. However it is more convenient to keep all the terms separately, as in (6.4)–(6.13).

As the external pressure P_0 (atmospheric forcing, (6.9)) we take a simple cosine profile $\tilde{P}_0 \cos kx$. It is convenient to use a non-dimensional amplitude of the forcing

$$p = \tilde{P}_0/\rho c_0^2, \tag{6.15}$$

where

$$c_0 = (g/k + Tk)^{1/2} \tag{6.16}$$

is the phase speed of linear gravity–capillary waves. Changing p (or $\tilde{P}_0$) alters the properties of the system. The length scale of the forcing coincides with the wavelength of the dominant wave, so that parasitic capillaries are not affected directly by the external pressure. Clearly, other choices of pressure forcing are possible, but the limited aim here is to balance the viscous dissipation with the energy flux across the surface.

To solve the system (6.4)–(6.13) we discretize equations on the interval of ζ from 0 to 2π. The derivatives are calculated using (6.4), while the series in (6.4) is truncated. In most of the runs 100–400 terms are kept in the series. The integrals in (6.7) and (6.11) are evaluated using the trapezoidal rule. The procedure yields a finite set of algebraic equations in a_m, c and E, while ak and p are used as independent non-dimensional parameters. The wavelength λ, the coefficient of surface tension T and viscosity ν are assumed to be fixed. (This is different from regular steady gravity waves, for which the wave amplitude or the wave slope is the only parameter after fixing λ.)

The set is solved numerically by Newton's method. The Jacobian for each iteration is computed numerically. As an initial guess, we usually take a linear wave profile. For other cases, we use a previously calculated solution as the initial guess for other combinations of parameters. Newton's method converges in a broad range of ak and p. As a rule, for each p there is an upper limit of the wave slope ak, and for each ak there is a lower limit of the forcing amplitude p, for which solutions are found. The former constraint means that there are limits to the wave heights, while the latter indicates that there should exist a minimum external forcing necessary for the waves to remain steady and not decay.

In presenting the results, the level from which we measure y is chosen so that the mean free surface elevation becomes zero. Also, since there is a phase shift, say Θ, between the profile of the free surface and the pressure distribution, again for presentation we shift the origin of the coordinate in the x-direction to centre the wave profile in the presentation window. We will briefly discuss the significance of Θ, when giving a physical interpretation of the pressure forcing in §8.

7. Calculations of wave energy and wave dissipation

In this section we calculate the energy and energy dissipation associated with gravity–capillary waves. We introduce the full energy density of a surface wave as

$$E_W = E_K + E_G + E_T, \tag{7.1}$$

where E_K, E_G and E_T are the mean energy densities of the kinetic energy, potential energy due to gravity, and potential energy due to surface tension, respectively. To compute separate terms in (7.1) at leading order in γ, we can apply formulas known for ideal surface waves (see Lighthill 1978; Longuet-Higgins 1984; Balk 1996). These formulas are useful, provided we know the elevation of the free surface and the distribution of the potential on the surface as functions of the horizontal coordinate:

$$E_K = \frac{\rho c}{2\lambda}\int_0^\lambda Y\,\mathrm{d}\phi^i, \tag{7.2}$$

$$E_G = \frac{\rho g}{2\lambda}\int_0^\lambda Y^2\,\mathrm{d}X, \tag{7.3}$$

and

$$E_T = \frac{\rho T}{\lambda}\int_0^\lambda ((1+Y_X^2)^{1/2}-1)\,\mathrm{d}X. \tag{7.4}$$

Here, each energy density is obtained as the average over the wave period. The dimension of E_K, E_G and E_T is energy per unit area. The kinetic energy E_K is calculated in the laboratory frame of reference, while the average surface elevation must be zero:

$$\bar{Y} = \frac{1}{\lambda}\int_0^\lambda Y\,\mathrm{d}X = 0. \tag{7.5}$$

The errors in calculating the energy from (7.2)–(7.5) are proportional to γ^2 and, as such, neglected.

The rate of work $\dot{E}_W$ produced by the surface pressure (per unit area) can be easily calculated as

$$\dot{E}_W = \frac{c}{\lambda}\int_0^\lambda P_0\,\mathrm{d}Y = \frac{c}{\lambda}\int_0^\lambda \tilde{P}_0\cos(kX)\,\mathrm{d}Y. \tag{7.6}$$

Consequently, the rate of energy dissipation (the relative loss of energy in the wave in one wave period) is

$$\beta = \frac{2\pi}{\sigma}\frac{\dot{E}_W}{E_W}. \tag{7.7}$$

Note that in the field, the local balance between energy input from the wind and viscous dissipation may not hold exactly, since usually there is energy transfer between neighbouring waves in a wave group, or wave growth, or decay.

Another parameter important in characterizing gravity–capillary waves is the ratio of potential energies due to surface tension and gravity:

$$\alpha = E_T / E_G. \tag{7.8}$$

This parameter describes the strength of parasitic capillaries. For linear waves (see (8.3) below), using (7.3) and (7.4), $\alpha = Tk^2/g$. Any substantial increase from this value indicates the appearance of strong capillary waves. For brevity we will call α the relative potential energy.

Finally, all the integrals in (7.2)–(7.6) can be recalculated using ζ as the independent parameter instead of x. For example for E_K this yields

$$E_K = -\frac{c^2\rho}{4\pi}\int_0^{2\pi} Y \,\mathrm{d}\zeta. \tag{7.9}$$

8. Linear approximation and physical interpretation of the pressure forcing

From (6.4)–(6.13) we can easily obtain simple wave solutions in the linear approximation. Even though this approximation does not include parasitic capillary waves, it reveals a number of physical properties of the full nonlinear solutions and is useful in investigating the effects of the pressure forcing.

Following a Stokes hypothesis (see Lamb 1932), we assume that the first Stokes coefficient a_1 is $O(\epsilon)$, while other coefficients are $O(\epsilon^2)$ and smaller ($\epsilon \ll 1$). Also to comply with (6.13) we must choose a_1 as

$$a_1 = ak\,\mathrm{e}^{-\mathrm{i}\Theta}, \tag{8.1}$$

where Θ is the phase shift and Θ/k is the displacement of the maximum of the pressure forcing with respect to the wave crest. Thus the Stokes expansion (6.3) reduces at leading order to

$$Z^i \approx \frac{1}{k}(\zeta + \mathrm{i}a_1\,\mathrm{e}^{-\mathrm{i}\zeta}) \tag{8.2}$$

and

$$Y^i \approx a\cos(\zeta+\Theta) \approx a\cos(kx+\Theta). \tag{8.3}$$

This last expression actually solves the problem, once we find Θ and the wave speed c. Now using (6.6) and (8.3) and neglecting terms of order ϵ^2 gives

$$U^{i2} \approx c^2(1-2kY^i). \tag{8.4}$$

For small ϵ we obtain

$$1/R \approx -Y_{xx}, \quad 1/R^i \approx -Y^i_{xx}, \tag{8.5}$$

and from (6.7)

$$Y \approx Y^i - \frac{2\nu}{\chi}(\Theta^{\iota}_{\xi} - \Theta^{\iota}_{\xi}|_{x=0}). \tag{8.6}$$

For simplicity, we replace ν/c with ν/c_0, since the viscosity ν is small, and there is only a small difference between c and c_0.

Substituting (8.4)–(8.6) in Bernoulli's integral (6.5), taking into account (8.3), and separating different terms yields two equalities

$$E = \frac{c^2}{2} + \frac{2g\nu}{c_0}Y^i_x|_{x=0} \tag{8.7}$$

and

$$\left(c^2-\frac{g}{k}+\frac{T}{k}\partial_{xx}\right)Y^i+\frac{2\nu}{c_0}\left(c^2+\frac{g}{k}-\frac{T}{k}\partial_{xx}\right)Y^i_x=\frac{\tilde{P}_0}{k\rho}\cos kx, \tag{8.8}$$

where the operator ∂_{xx} denotes the second derivative with respect to x. Equation (8.8) is an ordinary differential equation for Y^i. Using (6.15) and (8.3) in (8.8) gives two constraints (or compatibility conditions), which can be expressed after some algebra as

$$c^2=c_0^2\left(1+\frac{p}{ak}\cos\Theta\right) \tag{8.9}$$

and

$$\cos\Theta^2+\frac{4\nu^2k^2}{c_0^2}\left(\cos\Theta+\frac{2ak}{p}\right)^2=1, \tag{8.10}$$

with

$$-\pi\leqslant\Theta\leqslant 0. \tag{8.11}$$

Now considering (8.10) as a quadratic equation for $\cos\Theta$ yields its discriminant D as

$$D=1+\frac{4\nu^2k^2}{c_0^2}\left(1-\frac{4a^2k^2}{p^2}\right). \tag{8.12}$$

Since the discriminant should be positive, for small p (8.12) leads to an approximate condition for steady linear solutions to exist:

$$p\geqslant\frac{4\nu k}{c_0}ak. \tag{8.13}$$

This means that for each ak the pressure amplitude should exceed a certain threshold, which is determined by finite dissipation in the wave. As we show below, the dissipation turns out to be much stronger for nonlinear waves, and for the full nonlinear solutions the lower limit in (8.13) is significantly larger. In fact, most of the solutions we are going to present will satisfy the condition

$$\frac{4\nu k}{c_0}ak\ll p\ll ak, \tag{8.14}$$

which conforms to (8.13), while keeping the pressure relatively small.

As long as (8.14) holds, (8.10) can be simplified to obtain two possible solutions Θ_1 and Θ_2 with

$$\cos\Theta_1\approx-1+\frac{1}{2}\left(\frac{4\nu k}{c_0}\frac{ak}{p}\right)^2 \tag{8.15}$$

and

$$\cos\Theta_2\approx 1-\frac{1}{2}\left(\frac{4\nu k}{c_0}\frac{ak}{p}\right)^2. \tag{8.16}$$

Together with (8.11), this gives

$$\Theta_1\approx-\pi+\frac{4\nu k}{c_0}\frac{ak}{p} \tag{8.17}$$

and

$$\Theta_2\approx-\frac{4\nu k}{c_0}\frac{ak}{p}. \tag{8.18}$$

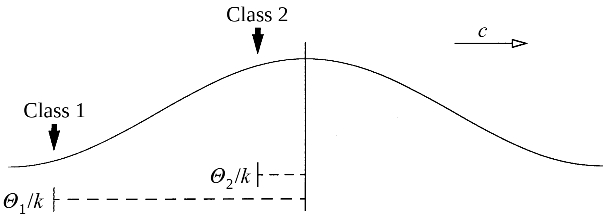

FIGURE 3. The profile of a linear sinusoidal wave with the locations of the maximum surface pressure for the Class 1 and Class 2 solutions. Note that in both cases the maximum of the surface pressure is applied on the rear face of the wave, leading to the air doing work on the water.

ak	p	ak	p
0.10	0.0003	0.30	0.016
0.15	0.0004	0.35	0.032
0.20	0.0027	0.40	0.049
0.25	0.0069	0.45	0.067

TABLE 1. The non-dimensional forcing amplitudes p in the numerical simulations of 5 cm waves.

This implies that there are two different classes of solution (Class 1 and Class 2, corresponding to Θ_1 and Θ_2). The main difference between the two is that for the first class, the surface pressure maximum occurs near the wave trough, while for the second class, it is near the crest. The pressure maximum is displaced slightly downwind from the trough for the Class 1 waves, and upwind from the crest for the Class 2 waves (figure 3). Such a shift is necessary for the pressure to transfer energy into the waves (see (8.19) below). Importantly, these two classes of solution will still exist in the nonlinear problem and will retain the basic properties we have just discussed.

The linear phase speed for the Class 1/Class 2 solution is smaller/larger than the linear phase speed in the absence of the forcing (see (8.9), (8.15) and (8.16)). Thus one of the effects of the pressure forcing is to reduce the speed of the Class 1 waves and increase it for the Class 2 waves. Note that the main effect of the pressure forcing is to supply energy to the wave to balance dissipation. That is why the physical properties of the Class 1 and Class 2 waves will be only slightly different as long as the pressure forcing remains relatively small.

To check the results for the linear approach we can calculate the linear dissipation rate. Substituting (6.15), (8.3) and (8.17) or (8.18) in (7.6) yields

$$\dot{E}_W \approx -\tfrac{1}{2}\rho p c_0^3\, ak \sin\Theta \approx 2\nu k^3 a^2 \rho c_0^2. \tag{8.19}$$

Calculating the full energy density of a surface wave gives

$$E_W \approx \tfrac{1}{2} k a^2 \rho c_0^2. \tag{8.20}$$

Thus the rate of energy dissipation per unit time is

$$\dot{E}_W / E_W \approx 4\nu k^2. \tag{8.21}$$

This is exactly the dissipation rate for surface waves on deep water from the classical linear theory (Phillips 1977; Lighthill 1978).

Now, based on the above analysis, we can give a physical interpretation of the

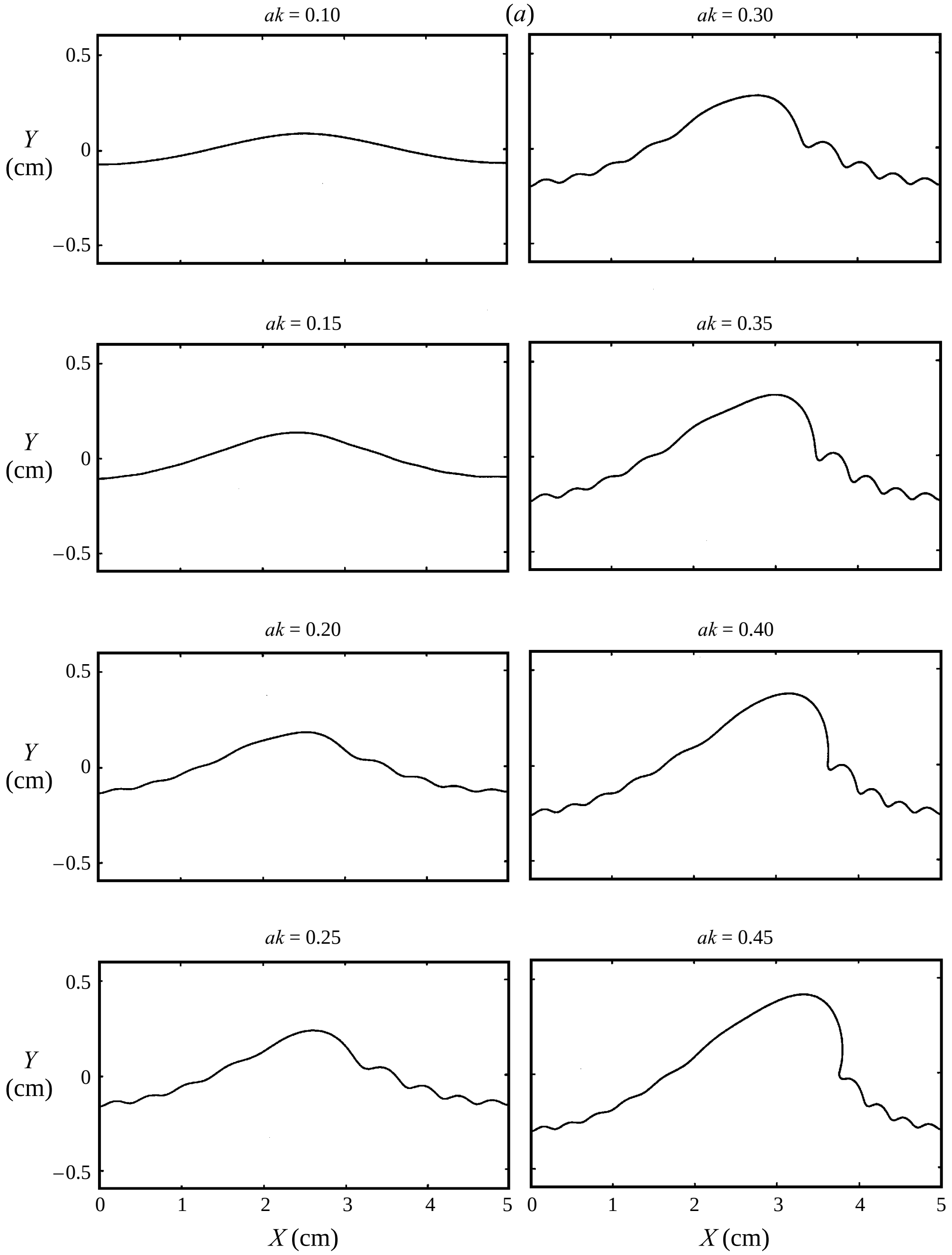

FIGURE 4(*a*). For caption see facing page.

pressure forcing. It is well recognized that the main mechanisms of wave generation in the ocean are connected with the direct or indirect action of the wind. For instance, in Phillips' (1957) model the energy of the stochastic turbulent fluctuations in the wind is transferred to the waves by the action of the normal pressure. In Miles' (1957, 1959) theory a shear flow in the air becomes unstable while blowing above a wavy water surface. As shown by Miles and confirmed by field measurements (Snyder *et al.* 1981)

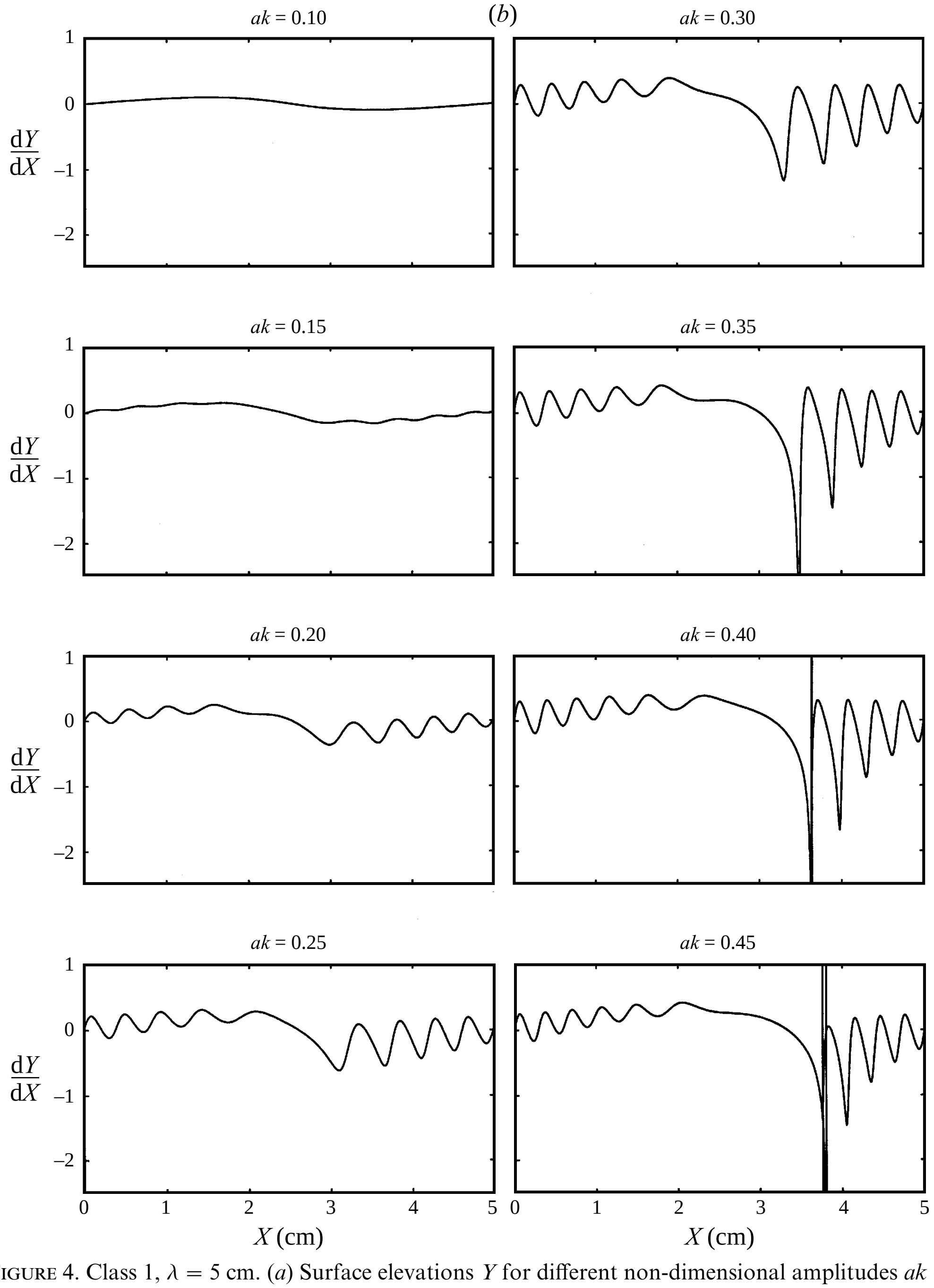

FIGURE 4. Class 1, $\lambda = 5$ cm. (*a*) Surface elevations Y for different non-dimensional amplitudes ak of the longer wave. Capillary ripples are clearly seen on the forward face of the surface wave. For $ak = 0.40$ and 0.45 the wave profiles are multi-valued, resembling waves close to breaking. (*b*) Surface slope $\mathrm{d}Y/\mathrm{d}X$ for different ak. The spikes in the plots for $ak = 0.40$ and 0.45 correspond to the multi-valued solutions.

the maximum aerodynamic pressure is located near the wave trough. When instability develops, a critical layer appears in the shear flow. Owing to the critical layer, the perturbation pressure becomes slightly shifted along the surface downwind as in figure 3. Thus we can associate our pressure forcing acting on the Class 1 solutions with the perturbation pressure in the Miles mechanism of wave generation.

In realistic conditions we can expect a pressure forcing to be more complex than a sinusoidal one and possibly even coupled with the wave field itself. Yet a cosine pressure distribution will be the simplest model to stimulate the effect of moderate wind on the waves.

In an alternative mechanism of wave generation, through the action of viscous forces on longer time scales, the wind produces a shear current in the water, which becomes unstable to surface wave modes (Morland *et al.* 1991). The physical mechanism of the instability in this case is similar to Miles' but now includes the presence of a critical layer in the water (Shrira 1993). Following the derivations by Shrira (see Appendix B), one can show that if the current is unstable the maximum perturbation pressure occurs slightly upwind of the wave crest. (The pre-condition for this analysis is a relatively weak shear current with no inflection points.) Therefore, the phase of the pressure forcing for the Class 2 waves is consistent with that for waves generated by a shear flow instability in the water.

9. Numerical results: 5 and 10 cm waves, Class 1 solutions

In this section we present numerical solutions of (6.4)–(6.13) with (6.15) for the Class 1 waves (associated with Miles' instability) that describe nonlinear gravity–capillary waves with forcing and dissipation for different non-dimensional wave amplitudes ak, or slopes of the longer waves. The parasitic capillary waves are prominent features of these solutions. The calculations are made for $\nu = 0.01\ \mathrm{cm^2\,s^{-1}}$ and $T = 73\ \mathrm{cm^3\,s^{-2}}$. The values of the non-dimensional amplitude of the forcing p are given in table 1. These value of p are close to, but slightly higher than, the minimum possible values of the pressure forcing for each ak, while the phase shift Θ varies roughly from $-\pi+\pi/7$ to $-\pi+\pi/4$ (cf. (8.17) for the linear model). Further, in §12 we discuss how the changes in the pressure forcing affect our solutions. It is important that even for larger ak the pressure forcing remains small ($p \ll ak$).

The ratio p/ak lies in the range $O(10^{-3}\text{–}10^{-1})$ with the upper limit slightly higher than the values resulting from Miles' (1959) calculations for a logarithmic wind profile and different winds.† However, we expect that larger values of p/ak and, consequently, a stronger pressure forcing can be provided by a stronger wind.

The elevation of the free surface Y and the wave slope $\mathrm{d}Y/\mathrm{d}X$ for 5 cm waves are presented in figures 4(*a*) and 4(*b*). The figures show how parasitic capillaries appear and become stronger on the forward face of the dominant waves with increasing wave amplitude. The number of capillary ripples increases as well. For very large amplitudes the wave profile becomes multi-valued, resembling overturning breaking waves. (We use the word multi-valued in the sense that Y expressed as a function of X is multi-valued. However, both $Y = Y(\zeta)$ and $X = X(\zeta)$ remain single-valued functions of ζ). A sharp corner develops separating the bulging crest and the train of capillary ripples. Although we neglected the rectified vorticity $\bar{\omega}$, it may in fact have some significant

---

† These values can be obtained from the relation connecting the aerodynamic pressure and the surface elevation (Miles 1957, equation (2.3)) and the numerical results for different wind speeds (Miles 1959, figures 4 and 5).

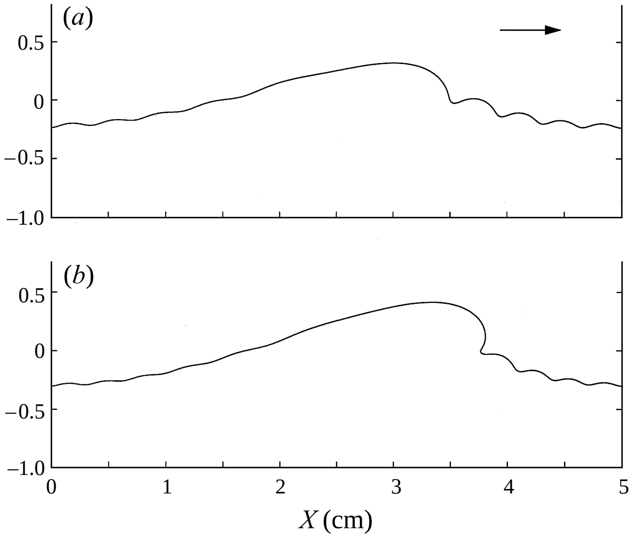

FIGURE 5. Class 1, $\lambda = 5$ cm; to scale. (*a*) A solution for $ak = 0.35$. This is a typical asymmetric gravity–capillary wave with damping. (*b*) A solution for $ak = 0.45$. This is a multi-valued solution, describing a wind-forced, damped gravity–capillary wave close to breaking.

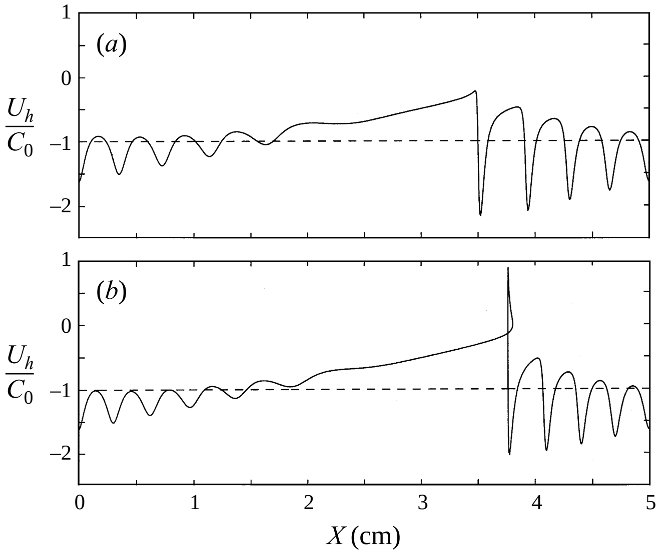

FIGURE 6. Class 1, $\lambda = 5$ cm. Plots showing the horizontal velocity U_h/c_0 at the surface. The flow accelerates significantly at the troughs of capillary ripples: (*a*) $ak = 0.35$; (*b*) $ak = 0.45$. A narrow loop in the plot corresponds to a multi-valued wave profile.

effect on the waves, including the separation of the flow near the sharp corner. In figures 5(*a*) and 5(*b*) we present the wave profiles for $ak = 0.35$, 0.45 with improved resolution and no vertical distortion.

To show the velocity field around the capillary ripples, we present several plots of dimensionless horizontal velocity U_h/c_0 at the surface as a function of the horizontal coordinate (figure 6). Clearly, the flow accelerates at the troughs of the capillary ripples, leading to a significant difference between the flow velocity and the linear phase

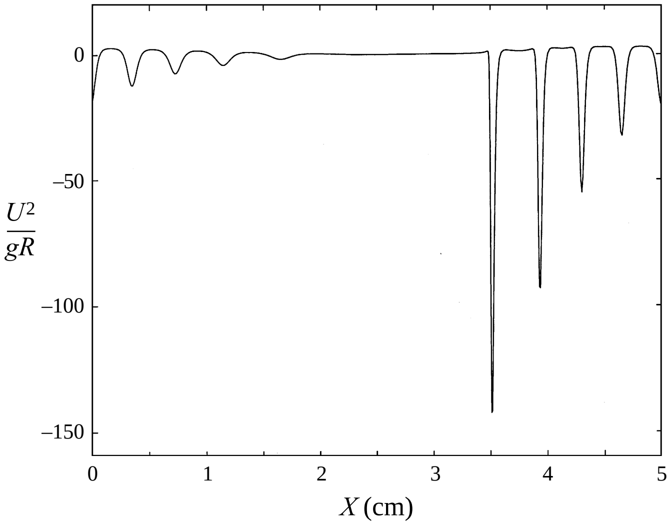

FIGURE 7. A plot showing local centripetal acceleration at the surface as a function of the horizontal coordinate for $ak = 0.35$. The acceleration is non-dimensionalized by the acceleration due to gravity. The minus sign corresponds to the outward direction from the water. Note the very high values of acceleration at the troughs of capillaries.

speed. A narrow loop in the plot for $ak = 0.45$ is consistent with a multi-valued wave profile. Note that in this case the horizontal velocity reaches zero twice, which corresponds to the limiting points of the wave profile where the fluid particles move vertically.

Although the flow velocity at the surface remains comparable with c_0, the radius of curvature in the troughs of capillary ripples may become very small (of order 10^{-1} mm). As a result, in the troughs of capillaries the centripetal acceleration of the flow, U^2/R, may exceed the acceleration due to gravity by many times (an example for $ak = 0.35$ is shown in figure 7). Importantly, despite the high local curvature, the profile remains smooth with no kinks or cusps, so that a truncated Stokes expansion still provides an adequate description of the surface. The smoothness of the profile is ensured by the dissipative terms, since any infinite curvature would create an infinite vorticity flux near the surface.

The most important parameters relevant for the computed surface waves are presented in figure 8 and include the dimensionless phase speed c/c_0, the ratio of potential energy due to surface tension and that due to gravity (relative potential energy) α, and the dissipation rate β. First, notice a slight increase in the phase speed when compared with linear waves. This increase is due to the effect of the nonlinear Stokes correction, partially counterbalanced by the effect of external forcing (see §8). The relative potential energy, α, rises with ak, but then experiences a significant decrease as soon as the wave profile becomes multi-valued. This drop is due to an increase in the absolute value of the gravitational potential energy and, to a lesser extent, to a decrease in the surface tension potential energy.

The dissipation rate β grows very rapidly with the wave amplitude and may exceed the values given by classical linear theory for the longer wave by two orders of magnitude. It is a strongly nonlinear function of the amplitude.

Now we proceed to our calculations for 10 cm waves. The values of the non-dimensional wave amplitude (or slope) ak and the amplitude of the forcing p are given

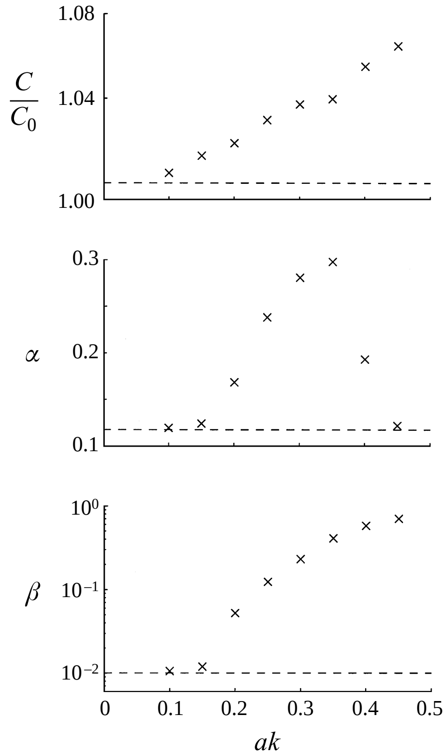

FIGURE 8. Class 1, $\lambda = 5$ cm. The phase speed c/c_0, the relative energy due to surface tension α, and the dissipation rate β versus ak. The values given by the classical linear theory for gravity–capillary waves are shown by dashed lines.

ak	p	ak	p
0.275	0.0005	0.35	0.0094
0.30	0.0006	0.375	0.0187
0.325	0.0025	0.40	0.0324

TABLE 2. The non-dimensional values of wave amplitude ak and amplitude of the forcing p in the numerical simulations of 10 cm waves.

in table 2. For these solutions the phase shift Θ varies roughly from $-\pi + \pi/9$ to $-\pi + \pi/25$. The surface elevation and slope are presented in figures 9(*a*) and 9(*b*). There are several differences in the properties of parasitic capillaries when compared with the 5 cm waves. The wave profiles for $ak = 0.35$, 0.40, with improved resolution and no vertical distortion, are shown in figures 10(*a*) and 10(*b*). Clearly, the capillary waves appear for higher amplitudes of the dominant waves. The capillaries are shorter, and more ripples develop. Another difference is the lack of capillary waves in the troughs of the longer waves.

Pertinent wave parameters are combined in figure 11, including the phase speed c/c_0, the relative potential energy α, and the dissipation rate β. Again, there is a slight departure from the linear phase speed, and a large increase in dissipation rates. Like the 5 cm waves, the relative potential energy rises, but with the transition to multi-valued profiles α decreases.

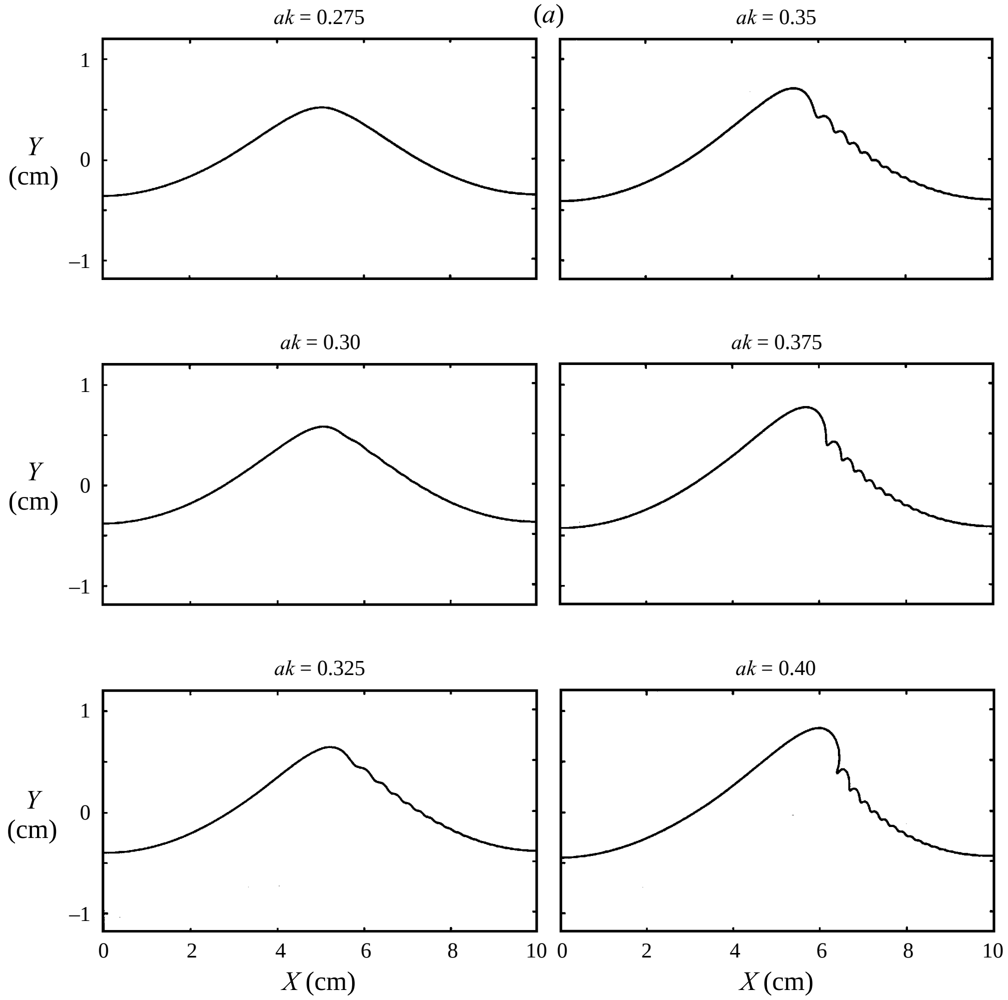

FIGURE 9(*a*). For caption see facing page.

To conclude this section, several important remarks are in order. With the increase of the wave amplitude and transition to a 'multi-valued' profile, the absolute slope $\mathrm{d}Y/\mathrm{d}X$ formally approaches infinity at several points of the profile, yet the functions $Y = Y(\zeta)$ and $X = X(\zeta)$ used in the derivations of the boundary layer relations remain well-behaved and confined. This implies that the relative slope of the wave ϵ, defined as in (2.26)–(2.27), remains small (definitely smaller than 0.5, which can be seen in figures 5 or 10). This formally justifies the use of a weakly nonlinear approximation for damping terms (and only damping terms).

Where our approximation can break down is in the steepest troughs of capillary waves for higher amplitudes of the dominant wave. We could choose the parameter $|1 + U_h/c_0|$ to describe local nonlinearity in the problem. For the linear problem it is much smaller than unity, as long as $U_h \approx -c_0$. For the nonlinear problem one can notice (figure 6) that, although this parameter remains relatively small along most of the wave profile, it may reach and even exceed unity in the steepest capillary troughs. The ratio of the boundary layer thickness to the radius of curvature of the surface, δ/R, which has been assumed to be small, may also reach unity. Thus higher-order nonlinear

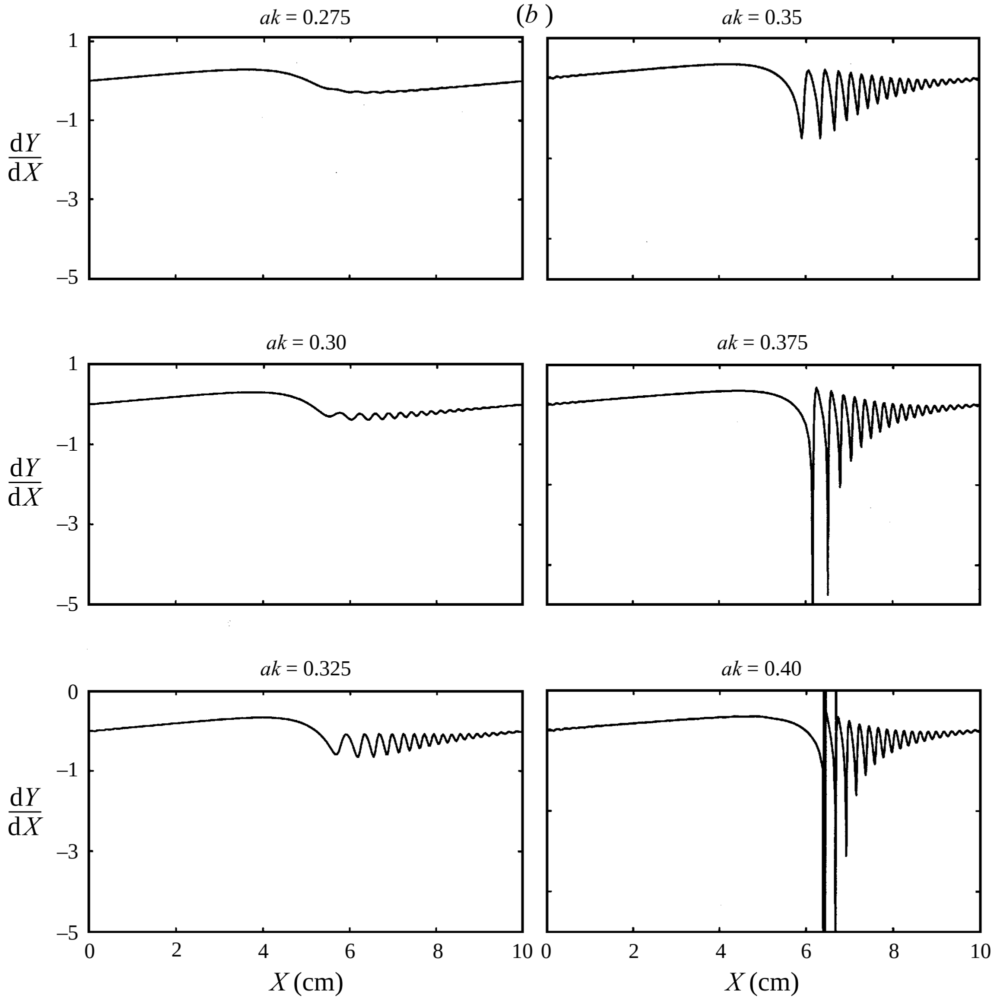

FIGURE 9. Class 1, $\lambda = 10$ cm. (*a*) Surface elevations Y for different non-dimensional amplitudes ak of the longer wave. Capillary ripples are clearly seen on the forward face of the surface wave. For $ak = 0.40$ the wave profile is multi-valued, resembling waves near breaking. (*b*) Surface slope $\mathrm{d}Y/\mathrm{d}X$ for different ak for 10 cm waves. The spikes in the plot for $ak = 0.45$ correspond to a multi-valued solution.

dissipative terms could become important, and this may limit the applicability of our results for greater amplitudes.

10. Spectral properties of computed gravity–capillary waves: Class 1 solutions

The most convenient spectral characteristics of the solutions computed in §9 can be obtained in terms of the Stokes coefficients a_m. First notice that the slope of the free surface is described by the function Z_ζ and to leading order in γ

$$kZ_\zeta - 1 = \sum_{m=1}^{\infty} m a_m \,\mathrm{e}^{-\mathrm{i}m\zeta}. \tag{10.1}$$

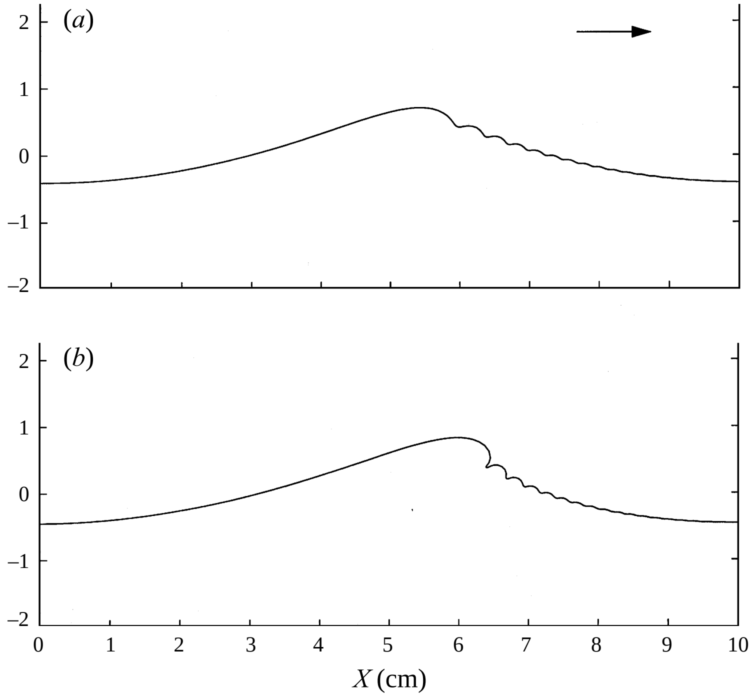

FIGURE 10. Class 1, $\lambda = 10$ cm. (a) A solution for $ak = 0.35$, to scale. This is a typical asymmetric gravity–capillary wave with damping. (b) A solution for $ak = 0.40$, to scale. This is a multi-valued solution, describing a wind-forced gravity–capillary wave with damping close to breaking.

Now it is natural to introduce spectral energy coefficients μ_m associated with (10.1)

$$\mu_m = m^2 a_m^* a_m. \tag{10.2}$$

The plots of μ_m as a function of wavenumber mk are presented in figure 12(a, b) for 5 and 10 cm waves with different non-dimensional wave amplitudes ak (again for minimum pressure forcing, cf. §8). The lower-wavenumber region with a relatively slow decay of the coefficients corresponds to the first few harmonics of the gravity–capillary wave which are slightly affected by the pressure forcing. The first local maximum corresponds to the observed parasitic capillary waves. One can check that other local maxima are associated with the higher harmonics of the capillary maximum. The magnitude of each of these local maxima is significantly weaker than that of the first.

A sharp decrease develops after the first local maximum with μ_m abruptly decreasing by 2 to 8 orders of magnitude (figures 12 and 13). This rapid decrease appears to be similar to the cut-off observed in the measurements of wind-wave spectra by Jähne & Riemer (1990), Klinke & Jähne (1995, 1997). Combining the results of measurements in the sea and numerous experiments in several wind-wave channels they show that the observed cut-off wavenumbers range from 800 to 1400 rad m^{-1} (Klinke & Jähne 1997; Klinke 1996). The most typical cut-off wavenumber is 1000 rad m^{-1}, which corresponds to a wavelength of about 6 mm.

There is a difference between their measurements and our model. Instead of a discrete spectrum determined by the fundamental wave and its harmonics, wind waves have a continuous spectrum. Thus instead of one fundamental wave we may have a continuous distribution of ‘fundamental waves’. Nevertheless, the cut-off appears to be similar in these cases.

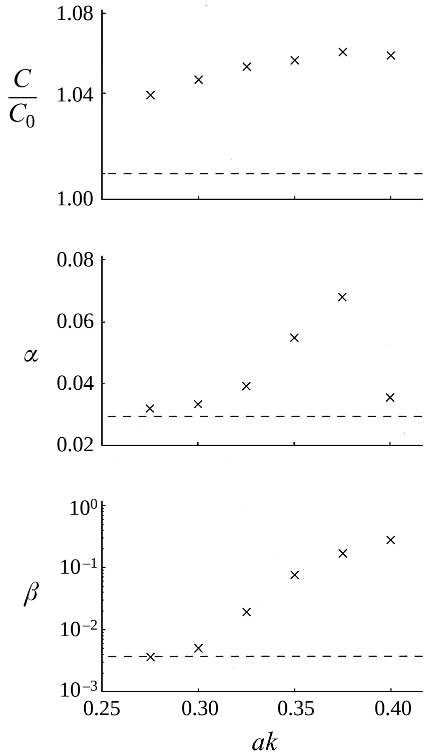

FIGURE 11. Class 1, $\lambda = 10$ cm. The phase speed c/c_0, the relative energy due to surface tension α, and the dissipation rate β versus ak. The values given by the linear theory for free surface waves are shown by dashed lines. Note that for lower values of ak, $(c-c_0)/c_0$ is proportional to ak and approaches zero as $ak \to 0$.

For our model we see that for 5 cm waves and moderate wave amplitudes, the cut-off occurs at approximately 1200–1300 rad m^{-1} (10th Stokes harmonic, figure 12*a*), which is in the range given by Klinke (1996). The cut-off wavenumbers increase a little for greater wave amplitudes. For 10 cm waves the cut-off wavenumbers are around 2500 rad m^{-1} (40th harmonic, figure 12*b*), somewhat larger than the laboratory and field measurements. The best agreement with the data of Klinke & Jähne is achieved for 4 cm waves and moderate wave amplitudes as can be seen from figure 13. The cut-off wavenumber is approximately 1000 rad m^{-1} (6th harmonic).

11. Numerical results: 5 cm waves, Class 2 solutions

As we mentioned above, the Class 1 and Class 2 gravity–capillary waves are very similar, differing mainly in the phase of the pressure forcing. As long as the pressure is relatively small, the main effect of the forcing is to do work on the wave to balance the dissipation. The forcing simply remains too weak to significantly influence other properties of the waves. Nonetheless, with the increase of the forcing amplitude several major differences emerge. In this section we briefly compare the Class 1 and Class 2 solutions for the minimum pressure forcing. Additional comparisons will be given in the next section, where we show that the effect of increased pressure will be qualitatively different for the two classes of waves.

As in §9, in figure 14 we show the elevation of the free surface for different wave

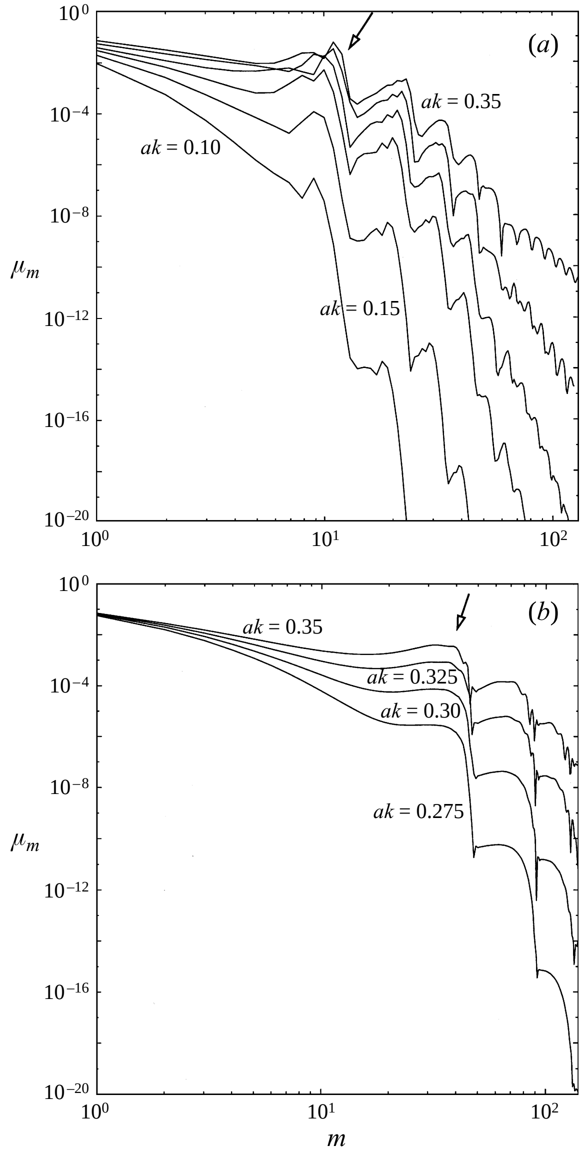

FIGURE 12. Class 1, (*a*) $\lambda = 5$ cm, (*b*) $\lambda = 10$ cm. Spectral energy coefficients μ_m as a function of the harmonic m for different ak. The first local maximum corresponds to parasitic capillary waves. A sharp drop (cut-off) in the magnitude of μ_m occurs after this maximum.

heights for both classes of waves. The amplitudes of the pressure forcing are the same as in table 1.† A more detailed comparison is given in figure 15. The main difference develops for larger wave heights, which correspond to stronger pressure forcing. Nevertheless, our solutions remain qualitatively very similar. Several pertinent wave parameters (phase speed, relative potential energy and dissipation rate) are presented in figure 16 for the Class 2 waves. Again, their behaviour is very similar to that of the

---

† The minimum forcing amplitudes necessary for steady solutions to exist are slightly different for the Class 1 and Class 2 waves. That is why some of the pressure amplitudes given in table 1 were chosen slightly higher than the actual minimum values.

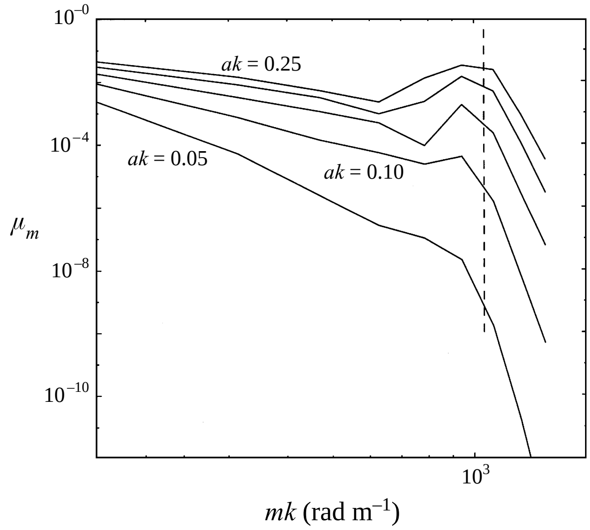

FIGURE 13. Class 1, $\lambda = 4$ cm. Spectral energy coefficients μ_m as a function of mk for different ak. Only coefficients for several first harmonics, including the first capillary maximum, are shown. A sharp decrease (cut-off) in the magnitude of μ_m occurs at approximately 1000 rad m^{-1} (cf. Klinke & Jähne 1995; Jähne & Klinke 1996).

Class 1 waves. An important difference is that now the deviation of the phase speed from the linear speed is significant, since both nonlinearity and the pressure forcing act to increase the phase speed.

12. The influence of increased pressure forcing on parasitic capillaries

In the previous section we used the minimum possible amplitudes of the forcing for each value of ak. From tables 1 and 2 and figures 4 and 9 it is easy to see that the increase in the pressure forcing accompanied by the increase in the amplitude of the longer wave necessarily leads to stronger parasitic capillaries (excluding multi-valued solutions). A question arises as to what happens if we increase the external pressure, while keeping the wave amplitude ak fixed. The answer will be quite different for the Class 1 and Class 2 waves. This is clearly seen from an example in figure 17, where we present 5 cm gravity–capillary waves with $ak = 0.25$ for different non-dimensional amplitudes of the forcing p.

Let us first consider the Class 1 waves. With an increase in the forcing, the capillary ripples become longer, and grow in amplitude (figure 17*a*). However, the situation is reversed for the Class 2 waves (figures 17*b*). The parasitic capillary waves shorten and become smaller, then almost disappear. The reason for this different type of behaviour is as follows. As we mentioned in §8, one of the effects of the pressure forcing is to reduce the phase speed of the Class 1 waves and increase it for the Class 2 waves. In figure 18 we give an example of how the phase speed c changes with an increase in p. Larger pressure amplitudes correspond to larger phase speeds for the Class 2 waves and smaller phase speeds for the Class 1 waves.

The capillary ripples appear due to the resonant magnification of higher harmonics of the fundamental wave. With any decrease of the phase speed of the dominant waves the resonant condition shifts towards longer and larger capillary waves (as for Class 1 waves), since longer capillary waves travel more slowly. Note that the Class 1 waves

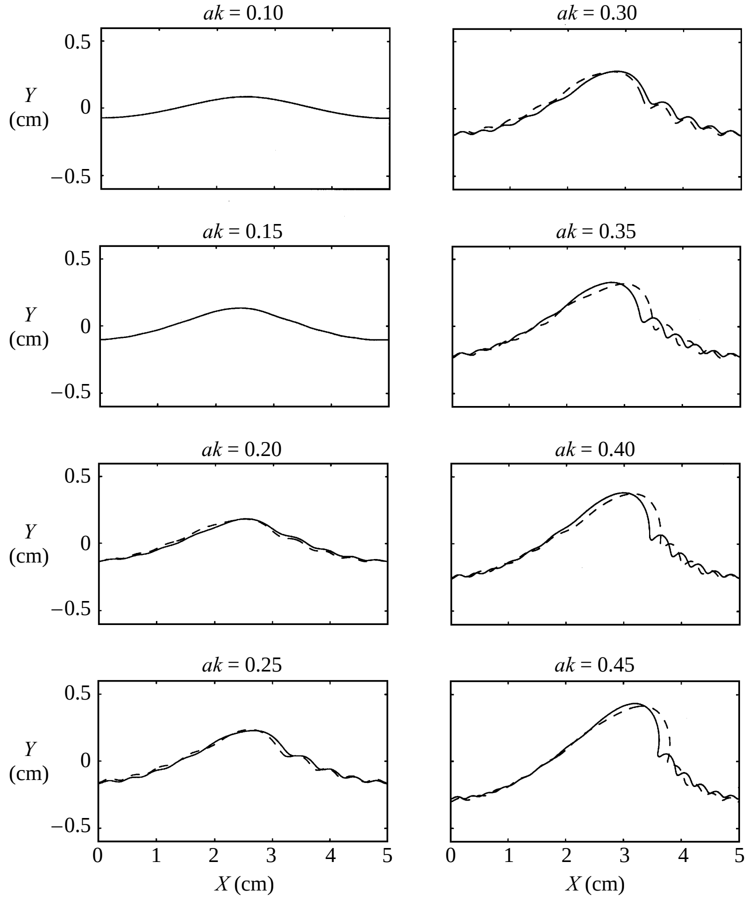

FIGURE 14. Class 2, $\lambda = 5$ cm. Surface elevations Y for different non-dimensional amplitudes of the longer gravity wave ak. Solid line, Class 2; dashed line, Class 1. The results are qualitatively very similar with the main difference appearing for higher wave amplitudes.

may even become subcritical. For the Class 2 waves the effect is reversed, and the phase speed increases with p, resulting in shorter capillary ripples. Shorter capillaries resonate with harmonics of a higher order, resulting in weaker capillary waves.

Finally, we found that there are no steady solutions of Class 1 for pressure amplitudes higher than some limiting value (in this particular case it is about 6.5 times greater than the minimum forcing amplitude). However, steady solutions of Class 2 still exist even for much stronger forcing. Nevertheless, both classes of waves appear to be relatively insensitive to changes of the pressure forcing, and a several-fold increase in p is needed for a qualitative change in the wave pattern.

13. Comparison with experiments

To test whether steady solutions obtained here are relevant to observations of quasi-steady gravity–capillary waves we conducted a short series of laboratory experiments. Here we present data from one experiment. A full account of our experimental work will be given in Fedorov, Melville & Rozenberg (1997). Measurements of mechanically generated gravity–capillary waves were made in a wave channel at the Hydraulics

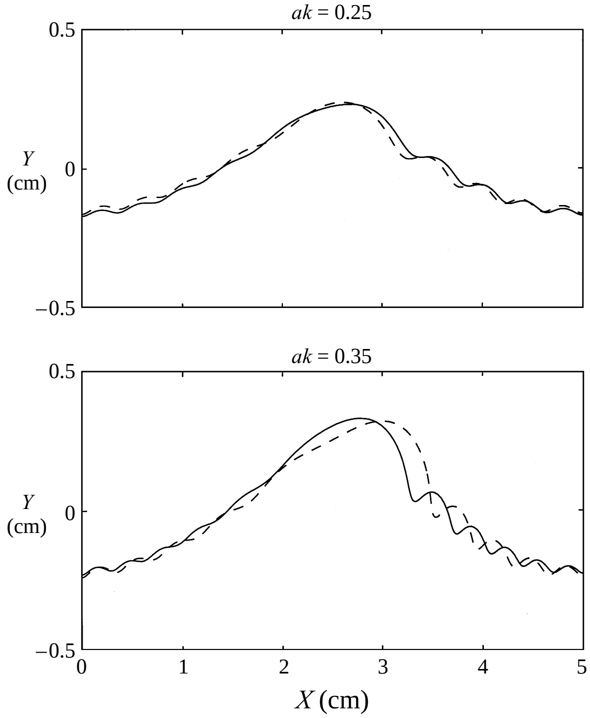

FIGURE 15. A detailed comparison of the Class 1 (dashed line) and Class 2 (solid line) solutions for $\lambda = 5$ cm. The difference is small for $ak = 0.25$, but significant for $ak = 0.35$.

Laboratory of Scripps Institution of Oceanography. The glass wave channel is 30 m long, 0.5 m wide and 0.6 m deep and is equipped with a wave maker (a wedge-shaped plunger). Data were taken at fetches greater than 1 m away from the wave generator. Measurements of the surface slope were made with a fixed laser slope gauge (LSG). This device uses the refraction of a laser beam by the water surface to measure the slope of the surface. To remove contaminants the surface of the channel was cleaned periodically by blowing wind and skimming the surface at the downwind end of the channel.

An example of a time series of surface slopes is shown in figure 19(*a*). The frequency of the dominant waves is 6 Hz, corresponding to a wavelength of approximately 5 cm. The wave pattern is almost periodic, which suggests local temporal stability; however, for time series greater than $O(1)$ second temporal unsteadiness becomes evident.

A fit with a solution obtained from our model is shown in figure 19(*b*). The calculations are made for $\lambda = 5.2$ cm, $ak = 0.20$ and $p = 0.0015$ (the Class 1 solutions, cf. figure 4*b*) and $\lambda = 5.1$ cm, $ak = 0.21$ and $p = 0.0076$ (the Class 2 solutions). Although we have achieved good agreement, there are some parameters in the experiments that we can only partially control (such as exact dissipation rates). Also note that the energy is transferred to the waves through the work of a wave generator, rather than through a pressure distribution at the surface. Consequently, the waves in the channel slowly decay, so that we can treat them as only quasi-periodic in space. This would lead to differences between the experimental measurements and the theory. On the other hand, the errors in the measurements are estimated to be in the range of 5–10 %, which is comparable to the differences between the observations and the numerical solutions.

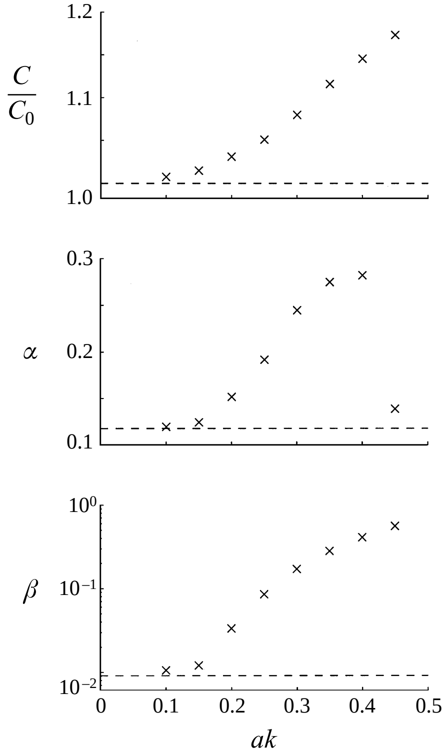

FIGURE 16. Class 2, $\lambda = 5$ cm. The phase speed c/c_0, the relative energy due to surface tension α, and the dissipation rate β, versus ak. The values given by the classical linear theory for gravity–capillary waves are shown by dashed lines.

It is noteworthy that the number of capillary ripples for this case (9 ripples) can be calculated almost exactly from the kinematics by applying the resonant condition and the linear dispersion relation. Since the linear phase speed is given by

$$c_0^2 = g/k + Tk, \tag{13.1}$$

we obtain

$$Tk^2 - c_0^2 k + g = 0, \tag{13.2}$$

which is a quadratic equation for k with two roots. The first one yields the dominant wave and the second one gives the capillary wave. Thus the characteristic wavenumber k_c for the capillary waves can be calculated as

$$k_c = \frac{c_0^2 + (c_0^4 - 4gT)^{1/2}}{2T}, \tag{13.3}$$

while the second root of (13.2) corresponds to the dominant wave. If these two roots are sufficiently separated (13.3) reduces to

$$k_c = \frac{\lambda}{2\pi}\frac{g}{T} \tag{13.4}$$

or

$$\lambda_c = \frac{4\pi^2}{\lambda}\frac{T}{g}, \tag{13.5}$$

where λ_c is the characteristic wavelength of the capillaries. The number of ripples M_c is

$$M_c \approx \frac{\lambda}{\lambda_c}. \tag{13.6}$$

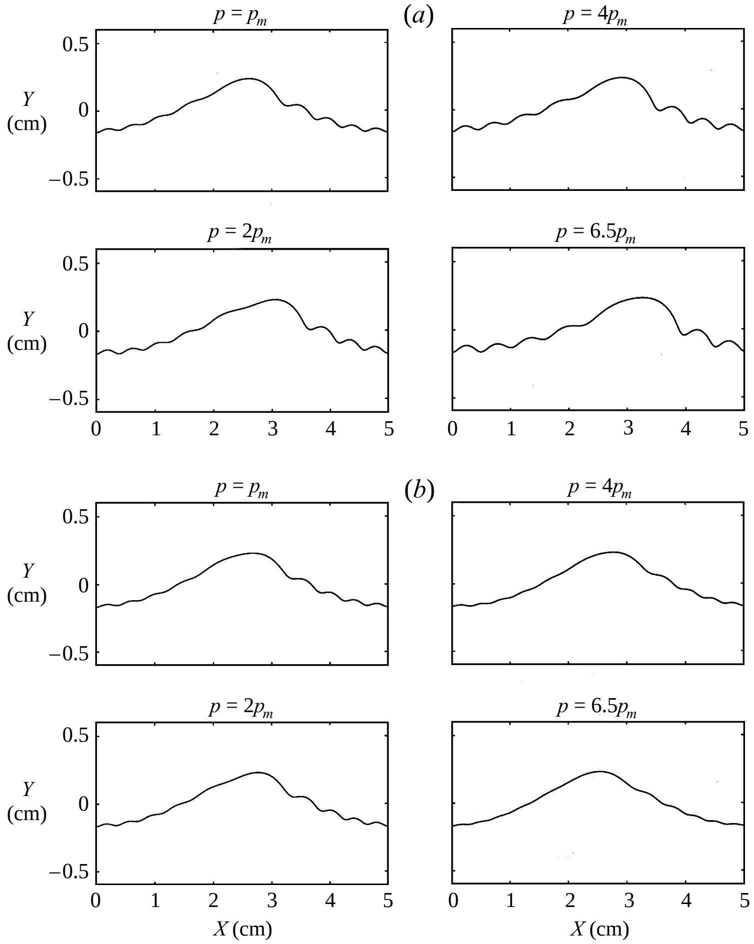

FIGURE 17. (*a*) Class 1, $\lambda = 5$ cm. Surface elevation for different pressure forcing for $ak = 0.25$. The amplitude of the forcing p varies from p_m to $6.5p_m$, where $p_m \approx 0.0069$ is the minimum forcing amplitude for $ak = 0.25$. See table 1. The parasitic capillary waves become stronger and a little longer with increased forcing. (*b*) As for (*a*) but Class 2. The parasitic capillary waves become much weaker and a little shorter with increased forcing. The ripples almost disappear for larger amplitudes of the forcing.

Substituting the value of the linear phase velocity based on the wavelength used in the model gives $M_c = 8.85 \approx 9$. Such good agreement suggests that for these parameters we are still within the range of the weakly nonlinear theory.

14. Conclusions

We have developed a theory of nonlinear gravity–capillary waves with forcing and dissipation. The theory is based on a boundary layer approximation and includes energy damping balanced by external pressure forcing. The approach reduces the problem of finding steady gravity–capillary waves to solving a set of algebraic equations via Newton's method. A prominent feature of the solutions is parasitic capillary ripples riding on the forward face of gravity–capillary waves.

Provided the pressure forcing is weak, there are two main classes of solutions. The

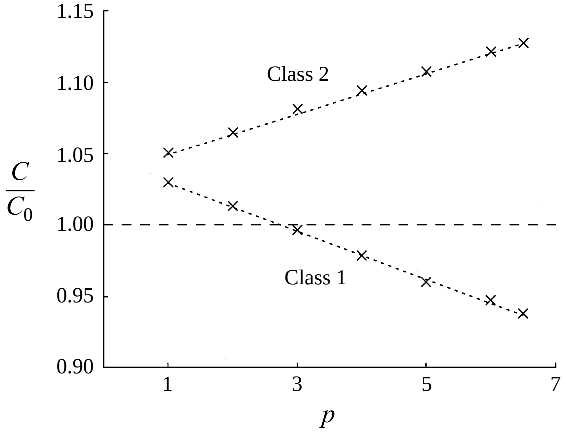

FIGURE 18. $\lambda = 5$ cm and $ak = 0.25$. The phase speed c/c_0 versus non-dimensional amplitude of the forcing p for the Class 1 and Class 2 solutions. The linear phase speed is shown by a dashed line. p is measured relative to p_m, where p_m is the minimum forcing amplitude. Notice that the Class 1 waves become subcritical with the increased forcing.

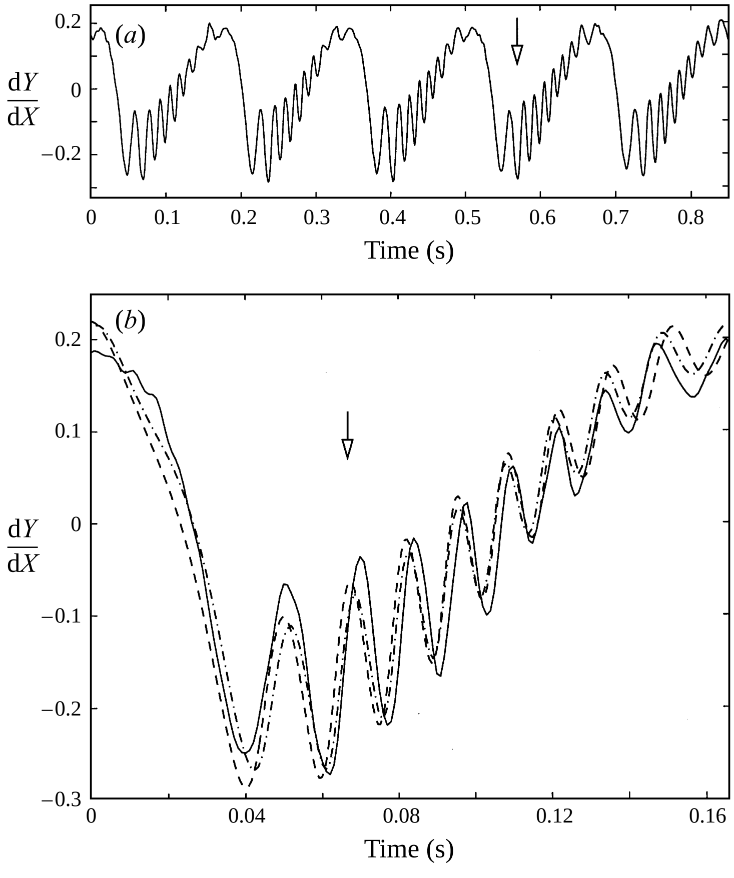

FIGURE 19. (*a*) Experimental measurements of the slope of mechanically generated 6 Hz waves in a channel. The measurements are taken as a function of time at a fixed point in space. (*b*) One period of the same time series compared with numerical solutions: $\lambda = 5.2$ cm, $ak = 0.20$ and $p = 0.0015$ (the Class 1 solutions, dashed line, cf. figure 4*b*), and $\lambda = 5.1$ cm, $ak = 0.21$ and $p = 0.0076$ (the Class 2 solutions, dot-dashed line).

major difference between them is that for the Class 1 waves the maximum surface pressure occurs near the wave trough, while for Class 2 it is near the wave crest. The Class 1 waves can be associated with Miles' mechanism of wind-wave generation due to a shear instability of the air flow above the water surface. The Class 2 waves are related to surface wave generation due to the instability of a shear current below the surface. Both classes of waves describe nonlinear gravity–capillary waves with weak forcing and dissipation and have a great degree of similarity. The properties of these solutions can be summarized as follows.

(i) Parasitic capillary waves appear on the forward face of the dominant waves, as long as the amplitude of the longer wave is sufficiently large. They rapidly become nonlinear. With the further increase of the amplitude of the longer wave the energy of capillary waves reaches a maximum, and, following the transition to a multi-valued profile, decreases.

(ii) Parasitic capillaries enhance the energy dissipation of the longer waves by 1–2 orders of magnitude, which conforms with previous conclusions of increased dissipation (Longuet-Higgins 1963; Ruvinsky *et al.* 1991), but the values given here are somewhat larger.

(iii) There is a cut-off (an abrupt decrease by several orders in magnitude) in the spectral energy density after the first local maximum corresponding to capillary ripples. The cut-off wavenumber for 4 cm dominant waves matches the most typical cut-off wavenumber measured by Jähne & Riemer (1990), Klinke & Jähne (1995, 1997).

(iv) There may be a significant change in the wave phase speed when compared to linear gravity–capillary waves. This deviation will be larger for the Class 2 waves and may reach as much as 20%. This may have important implications for the interpretation of microwave remote sensing of the oceans, which is commonly based on the kinematic properties of linear gravity–capillary waves.

(v) For a dominant wave of fixed height, the effect of the increased pressure forcing is to strengthen/weaken the capillary ripples for the Class 1/Class 2 waves.

(vi) When extended to very high wave amplitudes, the model produces multi-valued profiles, with a bulging-forward crest and a sharp corner in the wave profile which separates the crest and the train of parasitic capillaries. These solutions resemble gravity–capillary waves near breaking, but may be outside the region of the assumption of linear dissipation.

Finally, there is at least one other class of solutions (see Appendix A), which exists only with a strong pressure forcing ($p \sim ak$). The wave pattern for these Class 3 solutions consists of relatively flat surfaces separated by single ripples. This class of waves is physically different from the Class 1 or Class 2 solutions and is not topologically connected with either of them. An extensive analysis of this class of solutions will be given elsewhere.

Throughout this paper we have considered only two-dimensional waves; however, both laboratory and field data show that three-dimensional effects may become important (Zhang & Melville 1987). For example, both two- and three-dimensional modulational instabilities may render the pattern of capillary ripples unsteady, especially for greater wavelengths and wave amplitudes (Fedorov *et al.* 1997). Also, the waves could develop streamwise vortices, seen as streaks on the rear parts of the wave (Ebuchi *et al.* 1987). They may be related to a centrifugal instability caused by strong centripetal accelerations near the free surface.

Even in two dimensions, as the pressure forcing is increased, unsteady solutions may play an important role. For instance, steady solutions, especially those with overhanging wave crests, may develop instabilities. Also there may exist unsteady

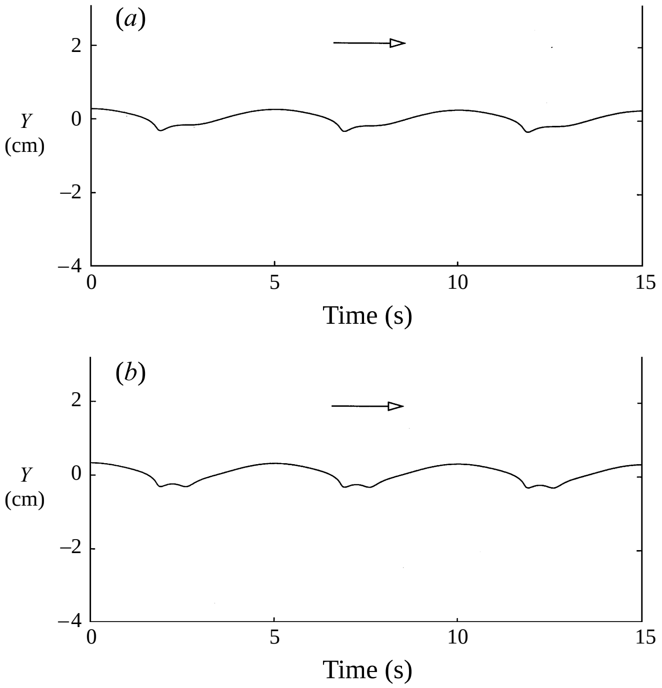

FIGURE 20. $\lambda = 5$ cm and $p \approx 0.19$. Strongly forced surface waves. The wave pattern consists of relatively flat surfaces separated by single capillary ripples. Several wave periods are shown with no distortion of the vertical scale. (*a*) $ak = 0.37$, (*b*) $ak = 0.40$.

solutions in the parameter range where no steady solutions can be found. These are subjects for future study.

We thank Anatol Rozenberg for permission to use the initial results of the experiments, and Michael Longuet-Higgins and John Miles for helpful advice and comments. We thank the reviewers for their suggestions which have led to many improvements in the paper. This work is supported by grants from the Office of Naval Research (Remote Sensing) and the National Science Foundation (Physical Oceanography).

Appendix A. Strongly forced solutions

As we mentioned above, there exist solutions additional to the Class 1 and Class 2 waves (say Class 3 waves). They appear only for relatively strong pressure forcing ($p \sim ak$). Without pursuing an extensive search for all possible solutions, we have found at least one completely different class of forced waves. This class is not topologically connected with the Class 1 or Class 2 solutions, and has rather different properties.

Here, we would like to demonstrate only two examples, shown in figure 20(*a*, *b*). In the first case the pattern consists of relatively flat surfaces separated by small single ripples, which locally resemble capillary solitons (Longuet-Higgins 1989; Zhang 1995). These ripples are likely to dissipate the main bulk of the energy supplied by the pressure forcing. In the second example with slightly larger wave amplitude (figure 20*b*), the capillary ripples look more like small capillary 'bumps', separating longer waves.

For both solutions the maximum pressure forcing occurs in the wave troughs. The phase speed of the waves reaches only about two thirds of the linear phase speed of the free gravity–capillary waves of the same length, which is due to the effect of the pressure forcing on the phase speed. The dissipation rate remains relatively high (20–30 % per period).

Appendix B. Perturbation pressure due to a subsurface shear current

Shrira (1993) considered small-amplitude gravity–capillary waves on subsurface shear currents. The problem is easily reduced to Rayleigh's equation with the appropriate boundary conditions. All the equations are linear and allow for monochromatic solutions. That is, the pressure P, the vertical velocity W, the elevation of the free surface η and other variables can be written as

$$\begin{pmatrix} P \\ W \end{pmatrix} = \begin{pmatrix} \hat{P} \\ \hat{W} \end{pmatrix} \mathrm{e}^{\mathrm{i}(kx-\sigma t)} \tag{B 1}$$

and

$$\eta = \hat{\eta}\, \mathrm{e}^{\mathrm{i}(kx-\sigma t)}, \tag{B 2}$$

where $\hat{P}$ and $\hat{W}$ are functions of the vertical coordinate y, and $\hat{\eta}$ is a constant. As usual in such problems, taking the real part of complex variables is implicitly required.

If the shear in the current is relatively weak in the sense given by (3.16/S) (hereafter S refers to Shrira 1993) and there are no inflection points in its profile, one can apply a formal perturbation method, expanding pertinent variables as follows:

$$\hat{P} = \hat{P}_0 + \hat{P}_1 + \dots, \quad \hat{W} = \hat{W}_0 + \hat{W}_1 + \dots, \quad \hat{\eta} = \hat{\eta}_0 + \hat{\eta}_1 + \dots, \tag{B 3}$$

$$\hat{c} = \hat{c}_0 + \hat{c}_1 + \dots, \tag{B 4}$$

where $\hat{c}$ is the complex wave phase speed. The zeroth-order terms in (B 3) and (B 4) describe a free surface wave carried by a uniform current, while the first-order corrections are due to the shear in the current. We assume that $\hat{c}_1$ has an imaginary part, which corresponds to unstable waves.

Using boundary conditions at the surface (equation (2.2/S)), we obtain several useful relations, including

$$\hat{\eta}_0 = \frac{\hat{W}_0^s}{\mathrm{i}k(U^s - \hat{c}_0)} \tag{B 5}$$

and

$$\hat{P}_1 = \rho c_0^2 \frac{\hat{W}_1^s}{\mathrm{i}(U^s - \hat{c}_0)}, \tag{B 6}$$

where $U = U(y)$ is the undisturbed profile of the current, and the superscript s indicates values calculated at the surface. Note that for unstable waves (Shrira 1993)

$$\hat{c}_0 \approx U^s - U_y^s/2k - c_0. \tag{B 7}$$

The zeroth-order solution that conforms with (B 5) and (4.1/S) can be taken as

$$\hat{W}_0 = \mathrm{e}^{ky}, \quad \hat{\eta}_0 = \frac{1}{\mathrm{i}k(U^s - \hat{c}_0)}. \tag{B 8}$$

For $\hat{W}_1^s$, applying (3.4/S) and (3.5/S), we obtain

$$\hat{W}_1^s = \frac{1}{2k} \int_{-\infty}^{0} \frac{U_{yy}}{U - \hat{c}} \mathrm{e}^{2ky}\, \mathrm{d}y \tag{B 9}$$

Using a conventional approach (Lin 1955; Miles 1957; Shrira 1993) that is valid if $\hat{c}$ has a small imaginary part gives

$$\hat{W}_1^s = \frac{1}{2k}\left(\mathrm{PV}\int_{-\infty}^{0} \frac{U_{yy}}{U-\hat{c}_0}\,\mathrm{e}^{2ky}\,\mathrm{d}y + \pi\mathrm{i}\,\frac{U_{yy}^c}{U_y^c}\,\mathrm{e}^{2ky_c}\right), \tag{B 10}$$

where PV stands for the principal value of the integral, and the index c shows the values calculated at the critical level, which is determined by $U(y_c) = \hat{c}_0$.

Now combining (B 6), (B 8) and (B 10) yields

$$\hat{P}_1 = (\hat{\alpha} + \mathrm{i}\hat{\beta})\rho c_0^2 k \hat{\eta}_0 \tag{B 11}$$

where

$$\hat{\alpha} = \frac{1}{2k}\mathrm{PV}\int_{-\infty}^{0} \frac{U_{yy}}{U-\hat{c}_0}\,\mathrm{e}^{2ky}\,\mathrm{d}y, \tag{B 12}$$

and

$$\hat{\beta} = \frac{\pi\mathrm{i}}{2k}\,\frac{U_{yy}^c}{U_y^c}\,\mathrm{e}^{2ky_c}. \tag{B 13}$$

Equation (B 11) is analogous to Miles' (1957) expression for the aerodynamic pressure above a wavy water surface. Note that the actual wave growth rate equals $\hat{\beta}c_0/\hat{c}_0$.

In the short-wave range $\hat{\alpha}$ can be estimated as

$$\hat{\alpha} \approx \frac{U_{yy}^s}{4k^2(U^s - \hat{c}_0)} \tag{B 14}$$

By Howard's semicircle theorem for unstable waves $U^s > \hat{c}_0$ (Yih 1972; Morland *et al.* 1991). Hence, $\hat{\alpha}$ is positive, so that (B 2) and (B 11) imply that the maximum perturbation pressure occurs near the wave crest. In turn, positive $\hat{\beta}$ implies that the maximum is displaced slightly upwind of the wave crest. Nevertheless, more study is necessary to establish a direct connection between the Class 2 waves and shear flow instabilities.

REFERENCES

Balk, A. M. 1996 A Lagrangian for water waves. *Phys. Fluids* **8**, 416–420.

Batchelor, G. K. 1967 *An Introduction to Fluid Dynamics*. Cambridge University Press.

Chen, B. & Saffman, P. G. 1980 Steady gravity–capillary waves on deep water. 2. *Stud. Appl. Maths* **62**, 95–111.

Cox, C. S. 1958 Measurements of slopes of high frequency wind waves. *J. Mar. Res.* **16**, 199–225.

Crapper, G. D. 1970 Non-linear capillary waves generated by steep gravity waves. *J. Fluid Mech.* **40**, 149–159.

Debiane, M. & Kharif, C. 1996 A new limiting form for steady periodic gravity waves with surface tension on deep water. *Phys. Fluids* **8**, 2780–2782.

Dommermuth, D. G. 1994 Efficient simulation of short and long-wave interactions with applications to capillary waves. *Trans. ASME: J. Fluids Engng* **116**, 77–82.

Dommermuth, D. G., Yue, D. K. P., Lin, W. M., Rapp, R. J., Chan, E. S. & Melville, W. K. 1988 Deep-water plunging breakers: a comparison between potential theory and experiments. *J. Fluid Mech.* **189**, 423–442.

Duncan, J. H., Philomin, V., Behres, M. & Kimmel, J. 1994*a* The formation of spilling breaking water waves. *Phys. Fluids* **6**, 2558–2560.

Duncan, J. H., Philomin, V., Qiao, H. & Kimmel, J. 1994*b* The formation of a spilling breaker. *Phys. Fluids* **6**, s2.

Ebuchi, N., Kawamura, H. & Toba, Y. 1987 Fine structure of laboratory wind-wave surfaces using an optical method. *Boundary-Layer Met.* **39**, 133–151.

Fedorov, A. V. & Melville, W. K. 1997 A study of rotational surface waves. (In preparation).

Fedorov, A. V., Melville, W. K. & Rozenberg, A. 1997 Experimental and numerical study of parasitic capillary waves. *Phys. Fluids* (submitted).

Jähne, B. & Riemer, K. 1990 Two-dimensional wave number spectra of small scale surface water waves. *J. Geophys. Res.* **95**, 11531–11546.

Klinke, J. 1996 Optical measurements of small-scale wind-generated water surface waves in the laboratory and the field. PhD thesis. University of Heidelberg. Germany.

Klinke, J. & Jähne, B. 1995 Measurements of short ocean waves during the MBL ARI West coast experiment. In *Air-Water Gas Transfer* (ed. B. Jähne & E. C. Monahan), pp. 165–173. AEON Verlag & Studi.

Klinke, J. & Jähne, B. 1997 Wave number spectra of short wind waves: a comparative study with data from wind-wave facilities and the field. *J. Phys. Oceanogr* (submitted).

Korn, G. A. & Korn, T. M. 1968 *Mathematical Handbook for Scientists and Engineers*. McGraw-Hill.

Lamb, H. 1932 *Hydrodynamics*. Cambridge University Press.

Landau, L. D. & Lifshitz, E. M. 1987 *Fluid Mechanics*. Pergamon Press.

Lighthill, M. J. 1978 *Waves in Fluids*. Cambridge University Press.

Lin, C. C. 1955 *The Theory of Hydrodynamic Stability*. Cambridge University Press.

Longuet-Higgins, M. S. 1953 Mass transport in water waves. *Phil. Trans. R. Soc. Lond.* A **245**, 525–581.

Longuet-Higgins, M. S. 1963 The generation of capillary waves by steep gravity waves. *J. Fluid Mech.* **16**, 238–159.

Longuet-Higgins, M. S. 1984 New integral relations for gravity waves of finite amplitude. *J. Fluid Mech.* **149**, 205–215.

Longuet-Higgins, M. S. 1989 Capillary-gravity waves of solitary type on deep water. *J. Fluid Mech.* **200**, 451–470.

Longuet-Higgins, M. S. 1992*a* Theory of weakly damped Stokes waves: a new formulation and a physical interpretation. *J. Fluid Mech.* **235**, 319–324.

Longuet-Higgins, M. S. 1992*b* Capillary rollers and bores. *J. Fluid Mech.* **240**, 659–679.

Longuet-Higgins, M. S. 1993 Capillary-gravity waves of solitary type and envelope solitons on deep water. *J. Fluid Mech.* **252**, 703–711.

Longuet-Higgins, M. S. 1994 Shear instabilities in spilling breakers. *Proc. R. Soc. Lond.* A **446**, 399–409.

Longuet-Higgins, M. S. 1995 Parasitic capillary waves: a direct calculation. *J. Fluid Mech.* **301**, 79–107.

Longuet-Higgins, M. S. 1996 Capillary jumps. *J. Phys. Oceanogr.* **26**, 1957–1965.

Longuet-Higgins, M. S. Dommermuth, D. G. 1997 Effect of surface tension on wave breaking. (submitted).

Lugt, H. G. 1987 Local flow properties at a viscous free surface. *Phys. Fluids* **30**, 3647–3652.

Mei, C. C. 1983 *The Applied Dynamics of Ocean Surface Waves*. John Wiley & Sons.

Miles, J. W. 1957 On the generation of surface waves by shear flows. *J. Fluid Mech.* **3**, 185–204.

Miles, J. W. 1959 On the generation of surface waves by shear flows. Part 2. *J. Fluid Mech.* **6**, 568–582.

Milinazzo, F. A. & Saffman, P. G. 1990 Effect of a surface shear layer on gravity and gravity-capillary waves of permanent form. *J. Fluid Mech.* **216**, 93–101.

Morland, L. C., Saffman, P. G. & Yuen, H. C. 1991 Waves generated by shear layer instabilities. *Proc. R. Soc. Lond.* A **433**, 441–450.

Mui, R. C. Y. & Dommermuth, D. G. 1995 The vortical structure of parasitic capillary waves. *Trans. ASME: J. Fluids Engng* **117**, 355–361.

Perlin, M., Lin, H. & Ting, C.-L. 1993 On parasitic capillary waves generated by steep gravity waves: an experimental investigation with spatial and temporal measurements. *J. Fluid Mech.* **255**, 597–620.

Phillips, O. M. 1957 On the generation of waves by turbulent wind. *J. Fluid Mech.* **2**, 417–445.

Phillips, O. M. 1977 *The Dynamics of the Upper Ocean*. Cambridge University Press.

RUVINSKY, K. D., FELDSTEIN, F. I. & FRIEDMAN, G. I. 1991 Numerical simulation of the quasi-stationary stage of ripple excitation by steep gravity-capillary waves. *J. Fluid Mech.* **230**, 339–353.

SHRIRA, V. I. 1993 Surface waves on shear currents – solution of the boundary-value problem. *J. Fluid Mech.* **252**, 565–584.

SNYDER, R. L., DOBSON, F. W., ELLIOTT, J. A. & LONG, R. B. 1981 Array measurements of atmospheric pressure fluctuation above surface gravity waves. *J. Fluid Mech.* **102**, 1–59.

WATSON, K. M. & BUCHSBAUM, S. B. 1996 Interaction of capillary waves with longer waves. Part 1. *J. Fluid Mech.* **321**, 87–120.

WATSON, K. M. & MCBRIDE, J. B. 1993 Excitation of capillary waves by longer waves. *J. Fluid Mech.* **250**, 103–119.

WHITHAM, G. B. 1974 *Linear and Nonlinear Waves*. John Wiley & Sons.

YIH, C. S. 1972 Surface waves in flowing water. *J. Fluid Mech.* **51**, 209–220.

ZHANG, X. 1993 A study of capillary and capillary-gravity wind waves: their structures, distributions, and energy balances. PhD thesis, Scripps Institution of Oceanography.

ZHANG, X. 1995 Capillary–gravity and capillary waves generated in a wind wave tank: observations and theories. *J. Fluid Mech.* **289**, 51–82.

ZHANG, X. & COX, C. 1994 Measuring the two-dimensional structure of a wavy water surface optically – a surface gradient detector. *Exps. Fluids* **17**, 225–237.

ZHANG, J. & MELVILLE, W. K. 1987 Three-dimensional instabilities of nonlinear gravity–capillary waves. *J. Fluid Mech.* **174**, 187–208.

ZUFIRIA, J. A. 1987 Non-symmetric gravity waves on water of infinite depth. *J. Fluid Mech.* **181**, 17–39.